JOURNAL OF GEOPHYSICAL RESEARCH, VOL. 102, NO. C6, PAGES 12,749–12,784, JUNE 15, 1997

Upper ocean thermohaline fields near 2°S, 156°E, during the Tropical Ocean-Global Atmosphere - Coupled Ocean-Atmosphere Response Experiment, November 1992 to February 1993

Adriana Huyer and P. Michael Kosro

College of Oceanic and Atmospheric Sciences, Oregon State University, Corvallis

Roger Lukas and Peter Hacker

School of Ocean and Earth Science Technology, University of Hawaii, Honolulu

Abstract. Zonal and meridional Seasoar sections centered at 1°50′S, 156°06′E were repeated >30 times in three 20-day periods between November 13, 1992, and February 15, 1993. Both sections were 130 km long, and sampling depth was 0–280 m, with a vertical resolution of ~2 dbar (2×10^4 Pa) and a horizontal resolution of ~3 km. The observed fields are complex and variable and are summarized graphically in several forms. Characteristics of the near-surface layer varied with the local winds which were variable and weak (< 6 m s^{-1}) during the first 20-day period, strong and westerly (>10 m s^{-1}) during much of the second, and moderate and westerly (4–10 m s^{-1}) during most of the third. Near-surface temperatures were warmest (up to 30°C) during the first period and coldest (often <29°C) during the second. Thermal stratification in the near-surface layer was strong under weak winds and weak under strong and moderate winds. Except during and after heavy rainfall, salinity stratification in the near-surface layer was generally weak. Surface salinity generally decreased toward the north. The depth of the surface isopycnal layer was often but not always limited by salinity stratification; the surface isohaline layer was shallower than the top of the thermocline throughout. Strong lateral temperature and salinity gradients occurred on a few occasions. Increased wind stress was associated with lateral homogenization as well as vertical mixing. Structure and water properties of the thermocline also varied between cruises and within each cruise. The upper thermocline was shallowest in late January after prolonged easterly winds. Isotherms in the upper and midthermocline (20°–25°C) sloped generally upward to the north, while those in the lower thermocline (12°–14°C) sloped down to envelop the core of the Equatorial Undercurrent, which shoaled (from 225 to 160 m) and warmed (from 15°to 20°C) between the first and last survey periods. Mesoscale and fine-scale water mass features were usually recognizable in sections less than a few days apart and migrated eastward at about 0.3 m s^{-1}. There is a remarkably high degree of nonstationarity in these thermohaline fields from the Warm Pool of the western Pacific Ocean.

1. Introduction

Progress in understanding ocean-atmosphere interaction in the warm pool of the western equatorial Pacific Ocean had been hindered by insufficient knowledge of the variability of both atmosphere and ocean over suitably small space scales and timescales, and a large international Coupled Ocean-Atmosphere Response Experiment (COARE), conducted as part of the Tropical Ocean-Global Atmosphere (TOGA) program, was designed to fill this vacuum. The program included complementary sampling of both atmosphere and upper ocean over a four-month intensive observation period (IOP) lasting from November 1992 through February 1993 [*Webster and Lukas,* 1992]. Both oceanographic and meteorological observations were concentrated in an intensive flux array (IFA) centered at 1°45′S, 156°00′E [*Webster and Lukas,* 1992; *Parsons et al.,* 1994]. The oceanographic component included studies of ocean mixing, measurements from surface

Paper number 97JC00267.
0148-0227/97/97JC-0267$09.00

and subsurface moorings, and both current and hydrographic observations from several stationary ships and a few survey ships [*Moum and Caldwell,* 1994; *Webster and Lukas,* 1992]. As part of COARE, we made frequently repeated high-resolution hydrographic observations during three month-long cruises of the R/V *Wecoma* to study the horizontal structure of time-varying upper ocean thermohaline and velocity fields at the center of the IFA; these surveys were designed to resolve zonal and meridional scales of 10 to 100 km and timescales of a few days to a few months. Results described in this paper show that temperature and salinity fields were remarkably nonstationary, both in the surface layer and in the main thermocline.

Each of the three *Wecoma* survey cruises (W9211A, W9211B, and W9211C) included measurements of the temperature, salinity, and velocity distribution in the upper 300 m of the ocean and continuous meteorological measurements of wind, air temperature, humidity, etc. Sampling focused on frequent repetition of a Standard Butterfly Pattern consisting of a meridional section along 156°06′W and a zonal section along 1°50′S, each 130 km long, connected by diagonal sections in the southwestern and northeastern quadrants of the COARE IFA (Figure 1, Table 1).

The center of our sampling pattern and of the COARE IFA, at ~ 1°45′S, lies about 160 km off the equator. This distance is less than the equatorial radius of deformation for first-mode baroclinic perturbations [*Gill,* 1982], and thus our repeated sections lie on the southern flank of equatorial phenomena such as the Equatorial Undercurrent and internal Kelvin waves. Historical observations in this region [*Toole et al.,* 1988; *Tsuchiya et al.,* 1989; *Richards and Pollard,* 1991; *McPhaden et al.,* 1992] and the average of 18 cross-equatorial sections made during COARE [*Eldin et al.,* 1994] all show the same basic structure as long sections made by *Wecoma*

Table 1. Positions of Apices and Intersection of the Standard Butterly Pattern Used for Seasoar Sections in the COARE Intensive Flux Array Throughout Most of the Three COARE Survey Cruises, W9211A (November 8 to December 8, 1992), W9211B (December 12 to January 16, 1993), and W9211C (January 22 to February 22, 1993)

Way point	Latitude	Longitude
SBN	1°14′S	156°06′E
SBS	2°26′S	156°06′E
SBW	1°50′S	155°30′E
SBE	1°50′S	156°42′E
I	1°50′S	156°06′E

Figure 2: a rather thick (>30 m) layer of very warm (>28°C) surface water extending many degrees north and south of the equator; isotherms in the thermocline (~14°–23°C) spreading apart within ~2°of the equator, away from the core (at ~200-m depth) of maximum eastward flow in the Equatorial Undercurrent (EUC); and a subsurface tongue of high-salinity South Pacific water tending northward across the equator at a depth of ~150 m, with maximum salinity decreasing from >35.6 psu at 5°S to ~34.8 psu at ~5°N and interleaving layers extending meridionally for >100 km. The typical width of the EUC seems to be about 200 km, typical core velocities are 0.3–0.5 m s^{-1}, and the center of the core usually lies between 1°N and 1°S [*Tsuchiya et al.,* 1989; *Richards and Pollard,* 1991; *McPhaden et al.,* 1992; *Eldin et al.,* 1994]. The strength of the EUC varies from <0.1 to >0.6 m s^{-1} on timescales of months [*McPhaden et al.,* 1990, 1992; *McPhaden,* 1993]. Our observations are consistent with this description of the EUC: eastward velocities of ~0.3 m s^{-1} in a broad core between 1°N and 1°S in early December and >0.6 m s^{-1} in an apparently narrow core near

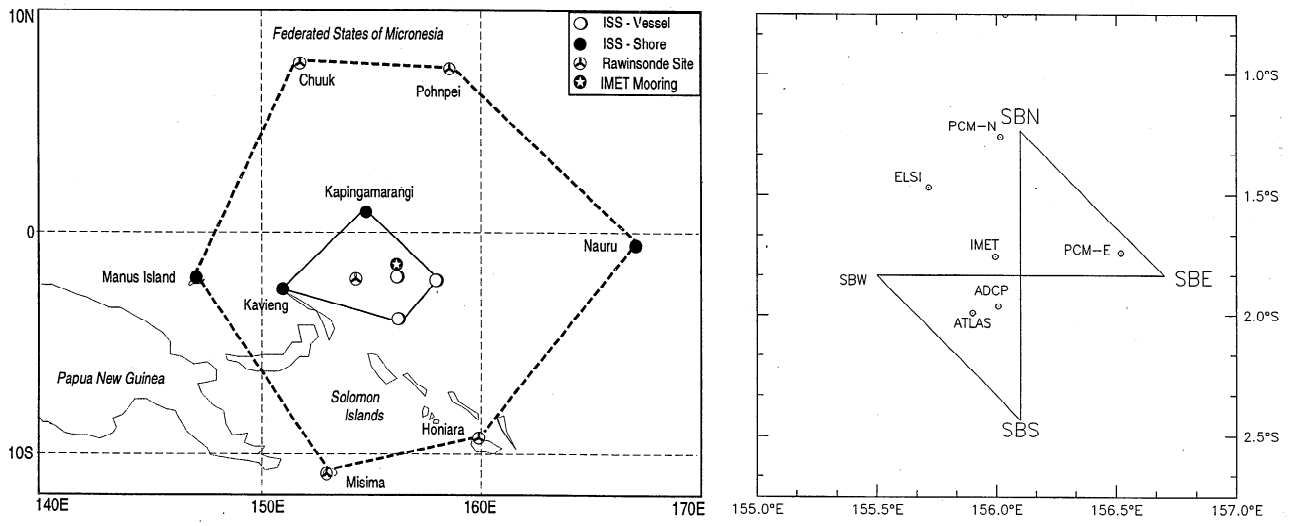

Figure 1. Location of the Standard Butterfly Pattern within the COARE outer sounding array (dashed lines, left panel) and the intensive flux array (solid lines, left panel), and its relation to the moorings near the center of the COARE intensive flux array (right panel).

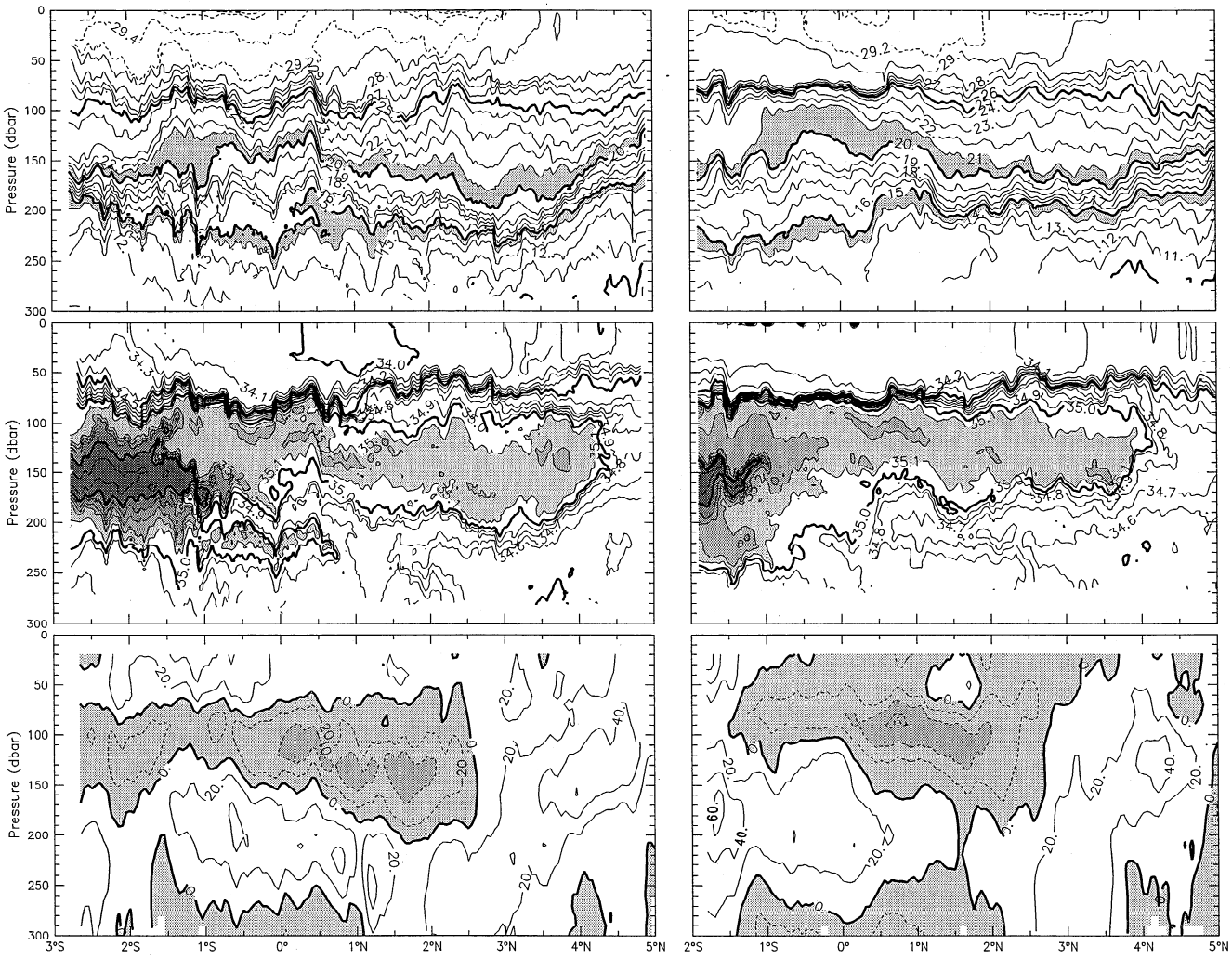

Figure 2. (top) Temperature, (middle) salinity, and (bottom) zonal velocity from long Seasoar/ADCP sections along 156.1°E: (left) December 1–3 and (right) January 10–12. Shading indicates temperatures of 14°–15°C and 20°–21°C; salinities of >35.2 (dark) and 35.1–35.2 (light), and westward flow (light, 0.0 to −0.4 m s^{-1}, dark, <0.4 m s^{-1}).

1°45′S in January (Figure 2). Above the EUC, there is usually a broader layer of westward flow with core velocities of ~0.3 m s^{-1}; this westward flow sometimes has a maximum at a depth of ~125 m [*Tsuchiya et al.*, 1989; *McPhaden et al.*, 1992] as it did in early December (Figure 2), and sometimes extends to the surface [*Tsuchiya et al.*, 1989; *Richards and Pollard*, 1991] as it did in January (Figure 2). Westward velocities of >0.4 m s^{-1} at the core (Figure 2) are within the range of historical values [*Tsuchiya et al.*, 1989; *McPhaden et al.*, 1992].

Historical observations indicate that equatorial surface salinities and surface currents are quite variable. Sometimes there is a local salinity maximum with values >35.0 psu on or near the equator [*Tsuchiya et al.*, 1989; *Richards and Pollard*, 1991; *McPhaden et al.*, 1992], presumably the result of equatorial upwelling. On other occasions, there is a local salinity minimum with values <34.1 psu [*Toole et al.*, 1988; *Tsuchiya et al.*, 1989], similar to the one observed during COARE (Figure 2) [*Eldin et al.*, 1994]; these low salinities seem to be associated with eastward surface currents and westerly winds [*McPhaden et al.*, 1992]. Equatorial surface currents are highly correlated with local winds, at least during periods of prevailing westerly winds; an eastward jet-like current ("Yoshida jet") with a width of ~200 km and core velocity of ~1.0 m s^{-} develops rapidly after the onset of westerly winds [*McPhaden et al.*, 1992].

The COARE IOP occurred within one of the longest El Niño-Southern Oscillation (ENSO) events on record [*Halpert et al.*, 1994]: the Southern Oscillation Index (SOI) fell below normal early in 1991 and remained so through at least October 1993. The SOI reached a deep minimum (indicating the mature phase of ENSO) in early 1992 and returned to near normal for a few months in mid-1992 before falling again in late 1992 [*Lukas et al.*, 1995b]. Large-scale monthly mean winds over the COARE domain were westerly during the mature phase

of ENSO in late 1991 and early 1992, easterly during the relaxation from ENSO between March and September 1992, near zero during the first half of the COARE IOP, and westerly again during the second half of the IOP [*Lukas et al.,* 1995b]. The 20°C isotherm shoaled by ~20 m in late 1991, during the mature phase of ENSO, and remained shallower than normal through the end of the COARE IOP [*Halpert et al.,* 1994; *McPhaden,* 1993; *Eldin et al.,* 1994].

The three *Wecoma* survey cruises within the COARE IOP were conducted under quite different weather regimes [*Weller and Anderson,* 1996]. Just prior to our surveys, there had been a prolonged burst of moderate westerlies in late October and early November. During our first survey period, winds were generally weak with net surface heating and little rainfall; these generally calm conditions were interrupted only by a brief burst of moderate westerlies on November 24–25. Low winds and net heating continued until December 10, when there was another burst of moderate westerly winds that ended a few days before the beginning of our second survey period. A series of three strong westerly wind bursts occurred between December 20 and January 2, coinciding with the first half of our second survey period; these were followed by calm winds and heavy rain. Between our second and third survey periods, winds were generally from the southeast, i.e., favorable for equatorial upwelling. Westerly winds resumed on January 27, at the beginning of our third survey period. Moderate westerly winds with frequent strong squalls prevailed from late January through the entire month of February.

In this paper we provide a summary of our hydrographic sampling and an overview of the spatial structure and temporal variability of the temperature, salinity, and density fields measured along the zonal and meridional sections. As this is the first hydrographic data set obtained from pumped Sea-Bird temperature and conductivity sensors in an undulating Seasoar vehicle, data acquisition and processing procedures are also summarized briefly in section 2. In section 3, we show overall time-averaged vertical sections along the meridional and zonal lines and discuss the average properties of the principal layers (surface layer, thermocline, thermostad, salinity maximum). In section 4, we compare cruise-averaged sections for each of the three survey periods, corresponding to three rather different weather regimes. In section 5, we examine the temporal variability on timescales of days to weeks by plotting the properties of selected isobars, isotherms, and isopycnals and discuss the behavior of the principal layers. The structure of the surface layer is further discussed in section 6, and the most important results are summarized in section 7.

2. Observations and Data Processing

The objective of our surveys was to measure the time-varying thermohaline fields of the upper ocean at the center of the COARE IFA, and our sampling plan was designed to resolve zonal and meridional scales of 10 to 100 km, vertical scales of a few meters, and timescales of a few days to a few months. The surveys were designed to complement time series observations from moorings and stationary ships: though fixed platforms provide better temporal resolution, they can resolve only a few spatial scales. We chose a butterfly pattern with its intersection as close as practical to the IMET mooring and nearly stationary R/V *Moana Wave* at the center of the IFA. The long sections of the butterfly were oriented in the zonal and meridional directions, parallel and transverse to the predominantly zonal equatorial currents, and connecting diagonal sections were in the northeast and southwest quadrants (Figure 1). Almost all of our sampling was done while underway at 7–8 knots (4 m s^{-1}), traveling south along the meridional (N2S) line and east along the zonal (W2E) section. Sampling included standard meteorological observations and underway current profiling, as well as upper ocean temperature and salinity measurements. The length of the orthogonal sections was limited to ~130 km to allow for completion of the entire pattern in <1.5 days, with multiple repetitions per week.

Since *Wecoma* was based in Guam, there was a long transit at the beginning and end of each cruise, and on some of these transits we were able to make a long cross-equatorial Seasoar section along 156°E (Figure 2); the remaining time (~20 days) was spent in the COARE IFA. During each of the three *Wecoma* cruises, we sampled repeatedly along the Standard Butterfly pattern (Figure 1, Table 1) with a towed undulating vehicle, Seasoar, equipped with a conductivity-temperature-depth (CTD) unit. The Seasoar vehicle, manufactured by Chelsea Instruments, resembles the vehicle described by *Pollard* [1986], but we used a Sea-Bird CTD with ducted temperature and conductivity sensors rather than a Neil Brown CTD. Seasoar towing speed was 7–8 knots (4 m s^{-1}). Minimum and maximum sampling depths were usually <3 m and >270 m, respectively. The cycling rate was 6–8 undulations per hour, yielding a horizontal resolution of <3 km. The Seasoar tows had a typical duration of 2–5 days. Details of the Seasoar operations have been presented in a series of data reports [*Huyer et al.*, 1993, 1994; *O'Malley et al.,* 1994]. Since this was the first field use of pumped Sea-Bird sensors in a Seasoar vehicle and conventional CTD processing procedures proved not to be fully adequate, sensor configuration and modified processing procedures are summarized here.

Seasoar was equipped with dual-ducted Sea-Bird (SBE) temperature (T) and conductivity (C) sensors mounted inside the nose, with intake and outlet ports (~0.05 m apart) on each side of the lower nose. Extra tubing between the intake and the standard SBE duct was ~0.08 m long. Water was pumped through each duct by an SBE submersible pump. Raw 24-Hz CTD data from Seasoar and unfiltered position and time data from the Global Positioning System (GPS) were ac-

quired and archived simultaneously. For in situ conductivity calibration, conventional CTD casts were made before and after each Seasoar tow, and salinity samples from *Wecoma*'s 5-m intake were collected once per hour. The sample data were paired with near-surface (3.0–5.5 m) Seasoar values, and conductivity corrections were determined from regression of Seasoar conductivity on sample conductivity, separately for each tow and sensor pair.

Lueck and Picklo [1990] have shown that salinities calculated from Sea-Bird ducted T-C sensors are subject to error from two main sources: a finite time lag between the temperature and conductivity measurements and a finite transfer of heat from the mantle of the conductivity cell to the water flowing through it. In a conventional SBE CTD, these errors are reduced by pumping the water through the ducted pair at a fixed rate and by applying a fixed T-C alignment offset and a thermal mass correction with fixed vales for the time constant and amplitude parameters to the raw 24-Hz data [Sea-Bird Electronics, 1992]. Even though we used the standard SBE duct with high-speed pumps, the flow rate through the sensors mounted inside the Seasoar vehicle was apparently not constant, presumably because of dynamic pressure gradients which varied with vehicle attitude and relative currents [*Huyer et al.*, 1993]. Cross correlation between 24-Hz T and C data indicated that the T-C lags (and flow rate) varied significantly and that the data should be realigned accordingly. *Morison et al.* [1994] have found that flow rate also affects the rate of heat transfer from the conductivity cell and conclude that both the amplitude parameter and the time constant of the thermal mass correction are related to flow rate. For the COARE data set, we found that varying the value of the amplitude constant was sufficient to remove most of the systematic difference between successive ascending and descending profiles, with no appreciable improvement from using a variable time constant.

The entire Seasoar data set was therefore reprocessed as follows: by calculating the T-C lags for consecutive data segments in specified depth ranges; using the time series of lags to offset the 24-Hz conductivity data relative to the temperature data within each segment; applying the appropriate conductivity calibration equations; applying *Lueck*'s [1990] correction for the thermal mass of the conductivity cell, with the value of the amplitude parameter related to the T-C offset for each data segment; and finally block averaging the data to 1-Hz values. Since the salinity data from descending profiles sometimes exhibited high-frequency noise that was absent from ascending profiles, we use only data from ascending profiles for all three cruises. We estimate the processed Seasoar CTD data to be accurate to ±0.01°C in temperature, ±0.01 psu in salinity, and ±1 dbar (±10 kPa) in pressure.

The basic Seasoar data set discussed in this paper consists of the 1-Hz temperature, salinity, and density data from ascending Seasoar profiles. A representative ensemble of vertical profiles for a single meridional (N2S) section from each cruise is shown in Figure 3. For some analyses, the data were placed on a fine-resolution

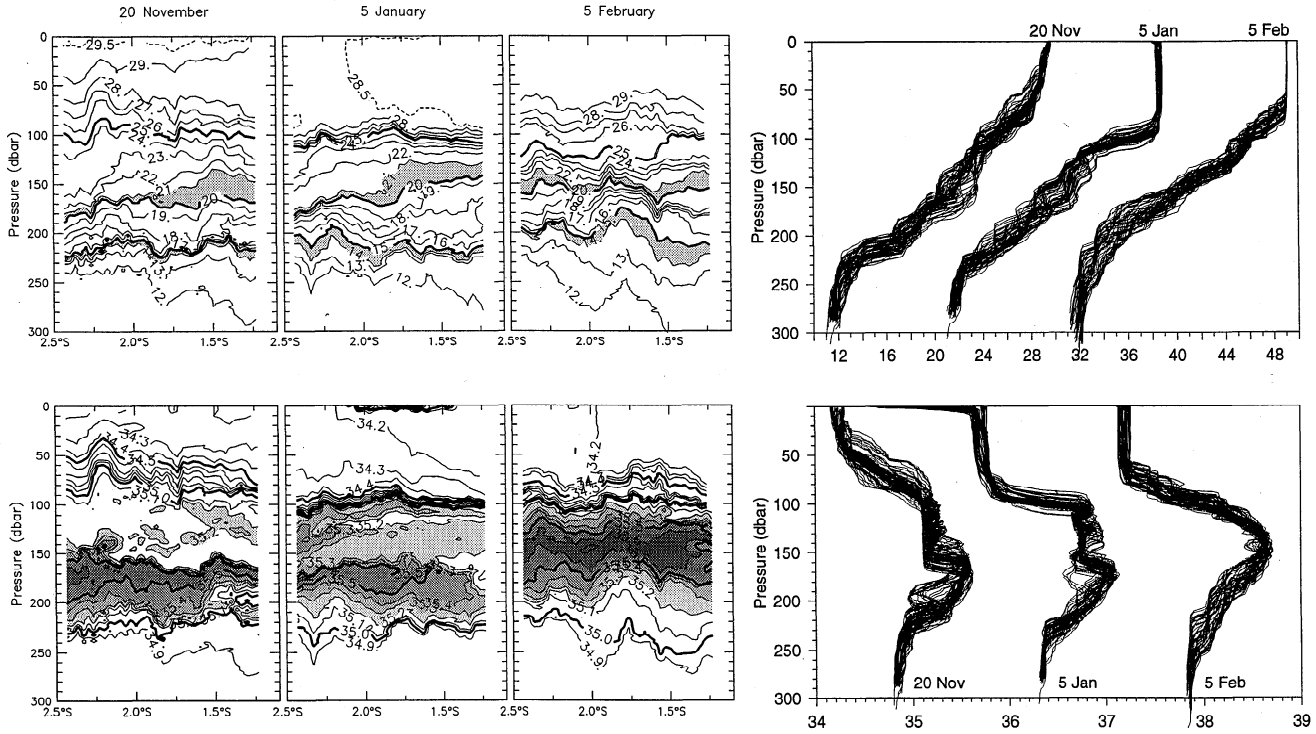

Figure 3. Samples of Seasoar data from the COARE IFA: (left) vertical distributions (plotted from 2-nm, 2-dbar gridded data) and (right) ensemble profiles (1-Hz data) of (top) temperature, and (bottom) salinity, for one N2S line from each cruise. Profile axis labels apply to the November 20 data; the January 5 profiles are offset by 10°C and 1.5 psu, and the February 5 profiles are offset by 20°C and 3.0 psu.

Table 2. Times of Complete Meridional (N2S) Sections of the Standard Butterfly Pattern

W9211A	W9211B	W9211C
0755 to 1938, Nov. 13[a]	1945, Dec. 20 to 0516, 21 Dec.	0917, Jan 27. to 1827, Jan. 27
0627 to 1534, Nov. 15	0553, Dec. 22 to 1653, Dec. 22	1930, Jan. 28 to 0430, Jan. 29
1652, Nov. 17 to 0118, Nov. 18	0346, Dec. 24 to 1323, Dec 24.	0945, Jan. 30 to 1926, Jan. 30
2325, Nov. 18 to 0754, Nov. 19	1138, Dec. 25 to 2120, Dec. 25	1827, Jan. 31 to 0358, Feb. 1
0605 to 1508, Nov. 20	1238, Dec. 27 to 2225, Dec. 27	0320, Feb. 2. to 1221, Feb. 2
1107 to 2032, Nov. 22	2209, Dec. 28 to 1721, Dec. 29[b]	0604, Feb. 4 to 1524, Feb. 4
1854, Nov. 23 to 0258, Nov. 24	1607, Dec. 30 to 0124, Dec. 31	1425, Feb. 5 to 0015, Feb. 6
0435 to 1431, Nov. 25	2358, Dec. 31 to 0922, Jan. 1	2200, Feb 7. to 0820, Feb. 8
1242 to 2215, Nov. 26	1349, Jan. 2 to 2316, Jan. 2	0803 to 1824, Feb. 9
2102, Nov. 27 to 0645, Nov. 28	1224, Jan. 3 to 2343, Jan. 3	1819, Feb. 10 to 0452, Feb. 11
2023 Nov. 29 to 0550, Nov. 30	1336 Jan. 5 to 2311, Jan. 5	0433 to 1456 Feb. 12
0421 to 1330, Dec. 1	2123, Jan. 6 to 0728, Jan. 7	0151 to 1139, Feb. 14
1734, Dec. 1 to 0229, Dec. 2[c]	1017, Jan. 8 to 2017, Jan. 8	

Times are given in UT. Almost all sections were southward along 15°06′E from SBN (1°14′S) to SBS (2°26′S).
[a]Northern portion of section was along 155°56′E.
[b]Section was interrupted by Seasoar recovery and deployment.
[c]Section was northward from SBS to SBN.

grid by block averaging horizontally over 2 minutes of latitude or longitude (2 nm) and vertically over either 2-dbar pressure bins (e.g., Figure 3) or over 0.1 kg m^{-3} increments of the density anomaly (σ_t). Although data tend to be relatively sparse near the surface, at depths >230 m, and at the extreme ends of each line, almost all 2-dbar grid points above 250 dbar were sampled in > 75% of the sections. The overall Seasoar data set from the three cruises includes a total of 38 complete sections along the meridional (N2S) line (Table 2) and 33 complete sections along the zonal (W2E) line (Table 3). Each section was usually completed in about 9 hours.

Upper ocean currents were measured along the ship's track [*Lukas et al.*, 1995a] with a 150-kHz RD Instruments acoustic Doppler current profiler (ADCP). Dual GPS receivers were used to determine ship's heading and to correct for gyro heading errors. The nominal depth range is 20–300 m. Vertical resolution was nominally 8 m, from data from 8-m bins with 16-m pulse length (W9211A) or 8-m pulse length (W9211B, C). The processed velocity data are accurate to better than 0.02 m s^{-1} on horizontal scales greater than 10 km.

3. Spatial Structure of Time-Averaged Fields

Although our sections are short (~130 km) compared to the equatorial radius of deformation (~200 km), significant horizontal structure is discernible in the time-averaged thermohaline fields. Time averages and temporal standard deviations for the entire three-cruise pe-

Table 3. Times of Complete and Nearly Complete Zonal (W2E) Sections of the Standard Butterly Pattern

W9211A	W9211B	W9211C
0814 to 1808, Nov. 14	2019, Dec. 19 to 0227, Dec. 20[a]	0143 to 1207, Jan. 28
0329 to 1038, Nov. 17[a]	1217 to 2048, Dec. 21	1646, Jan. 29 to 0225, Jan. 30
0723 to 1647, Nov. 18	0000 to 0827, Dec. 23	0238 to 1112, Jan. 31
1422 to 2310, Nov. 19	2026, Dec. 24 to 0455, Dec. 25	1124 to 2015, Feb. 1
0242 to 1206, Nov. 23	2017, Dec. 26 to 0526, Dec. 27	1410 to 2304, Feb. 3
0925 to 1755, Nov. 24	0532 to 1450, Dec. 28	2230, Feb. 4 to 0719, Feb. 5
2120, Nov. 25 to 0525, Nov. 26	0018 to 0846, Dec. 30	0747 to 1641, Feb. 6
0505 to 1353, Nov. 27	0826 to 1715, Dec. 31	1524, Feb. 8 to 0114, Feb. 9
1330, Nov. 28 to 1323, Nov. 29[b]	1602, Jan. 1 to 0007, Jan. 2	0200 to 1128, Feb. 10
1225 to 2123, Nov. 30	2230, Jan. 4 to 0639, Jan. 5	1207 to 2135, Feb. 11
	0603 to 1443, Jan. 6	0845 to 1856, Feb. 13
	1354 to 2234, Jan. 7	1833, Feb. 14 to 0456, Feb. 15
	0250 to 1139, Jan. 9	

Times are given in UT. All sections were easthward along 1°50′S from SBW (155°30′E) to SBE (156°42′E).
[a]Partial section only, completed with CTD stations.
[b]Section was interrupted by Seasoar recovery and deployment.

riod (November 13, 1992 to February 15, 1993) were calculated from both the 2-dbar pressure-gridded data and the 0.1 kg m^{-3} density-gridded data. Averages of pressure-gridded data (i.e., along isobars) are more appropriate for comparison with data from moored instruments and for studying layers with very weak stratification. Averages of density-gridded data (i.e., along isopycnals) are more appropriate for studying water mass characteristics. As might be expected from the close proximity to the equator, these fields show asymmetry in the meridional plane and lateral homogeneity in the zonal plane.

Vertical profiles of temperature, salinity, and density anomaly at the four corners of our sampling pattern Figure 4 show the characteristic structure of the western equatorial Pacific. The surface layer is rather thick (>30 m), very warm (>28°C), relatively fresh (<34.5 psu), nearly isothermal, and weakly stratified in salinity [*Lukas and Lindstrom,* 1991]; the surface salinity was slightly lower than normal and about the same as observed after strong westerly winds in early 1986 [*Eldin et al.,* 1994]. The very steep thermocline, with temperature decreasing >15°C in 200 m [*Toole et al.,* 1988], contains the broad subsurface salinity maximum [*Richards and Pollard,* 1991]; *Eldin et al.* [1994] note that the upper thermocline in this period was 10–40 m shallower than climatology, consistent with the ongoing El Niño conditions. The deep thermostad (250 to 300 m) is about 1°C colder than suggested by its historical name (Thirteen Degree Water [e.g., *Tsuchiya,* 1981]), which is more appropriate in the eastern Pacific. Statistics of the pressure-gridded temperature, salinity, and density (Figure 4) show maximum variability at depths with the strongest vertical gradients

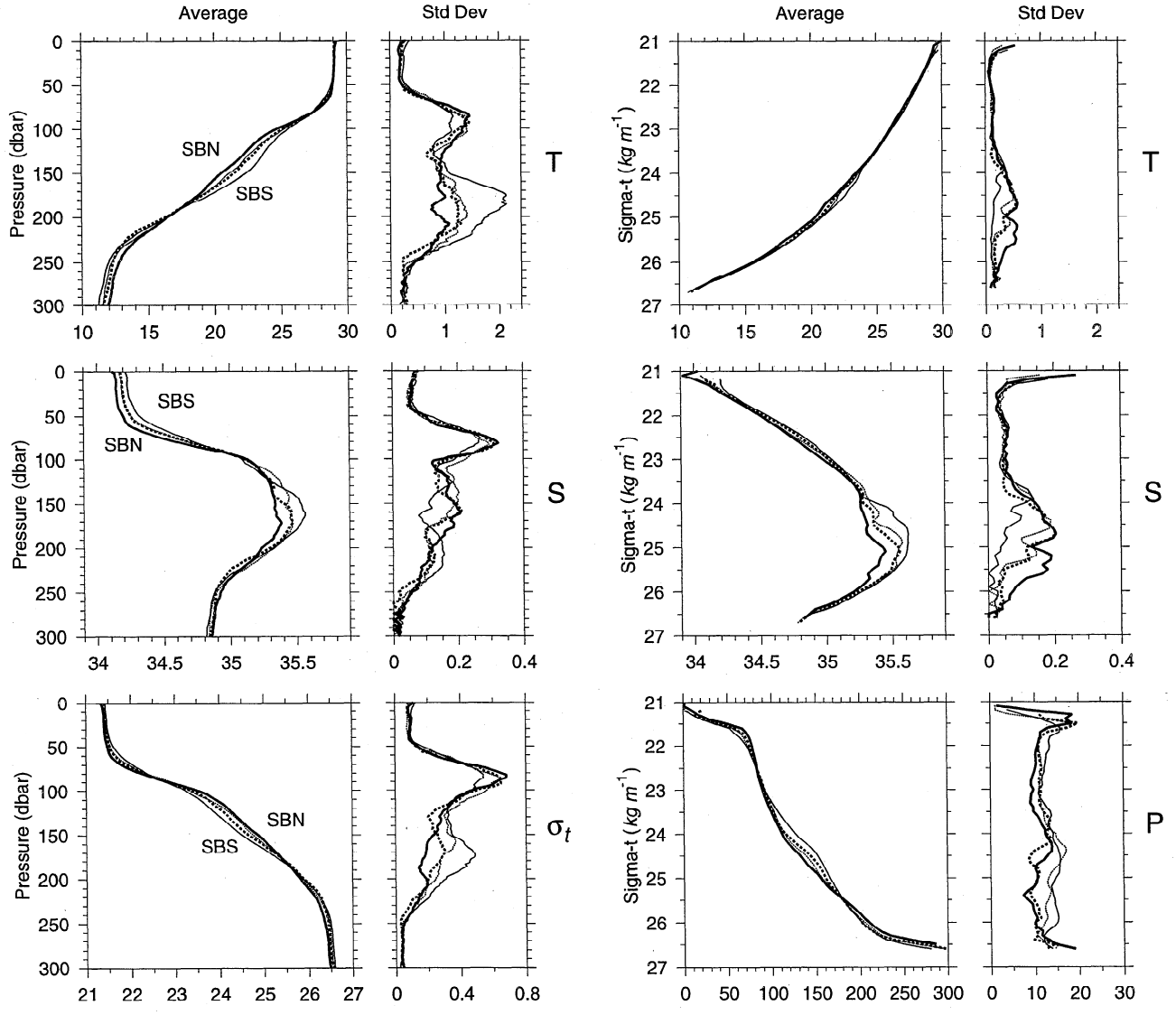

Figure 4. Profiles of the average and standard deviation of (top) temperature, (middle) salinity, and (bottom) sigma-t near the four corners: SBN (heavy line), SBS (thin line), SBW, (thin dotted line), and SBE (heavy dotted line). Statistics were calculated from both the (left) pressure-gridded data and (right) density-gridded data.

and the standard deviation of isopycnal displacement is 10–15 m through most of the water column (Figure 4). The isopycnal standard deviations of temperature and salinity are very small (<0.2°C, ~0.05 psu), except in the core of the salinity maximum (23.5 to 26.3 σ_t) and at the top of the surface layer (σ_t <21.5).

The average profiles for the four corners are remarkably similar (Figure 4): the profiles from the western and eastern corners do not differ significantly at any depth, and differences between the northern and southern corners are small at most depths. The surface layer has virtually the same temperature at all four locations: differences among profiles (<0.15°C) are less than the standard deviation at each location. Surface salinity is 0.05 psu higher in the south (at SBS) and 0.05 psu lower in the north (at SBN) than at either the western (SBW) or eastern (SBE) corners; this latitudinal salinity gradient might be expected from the usual position of the

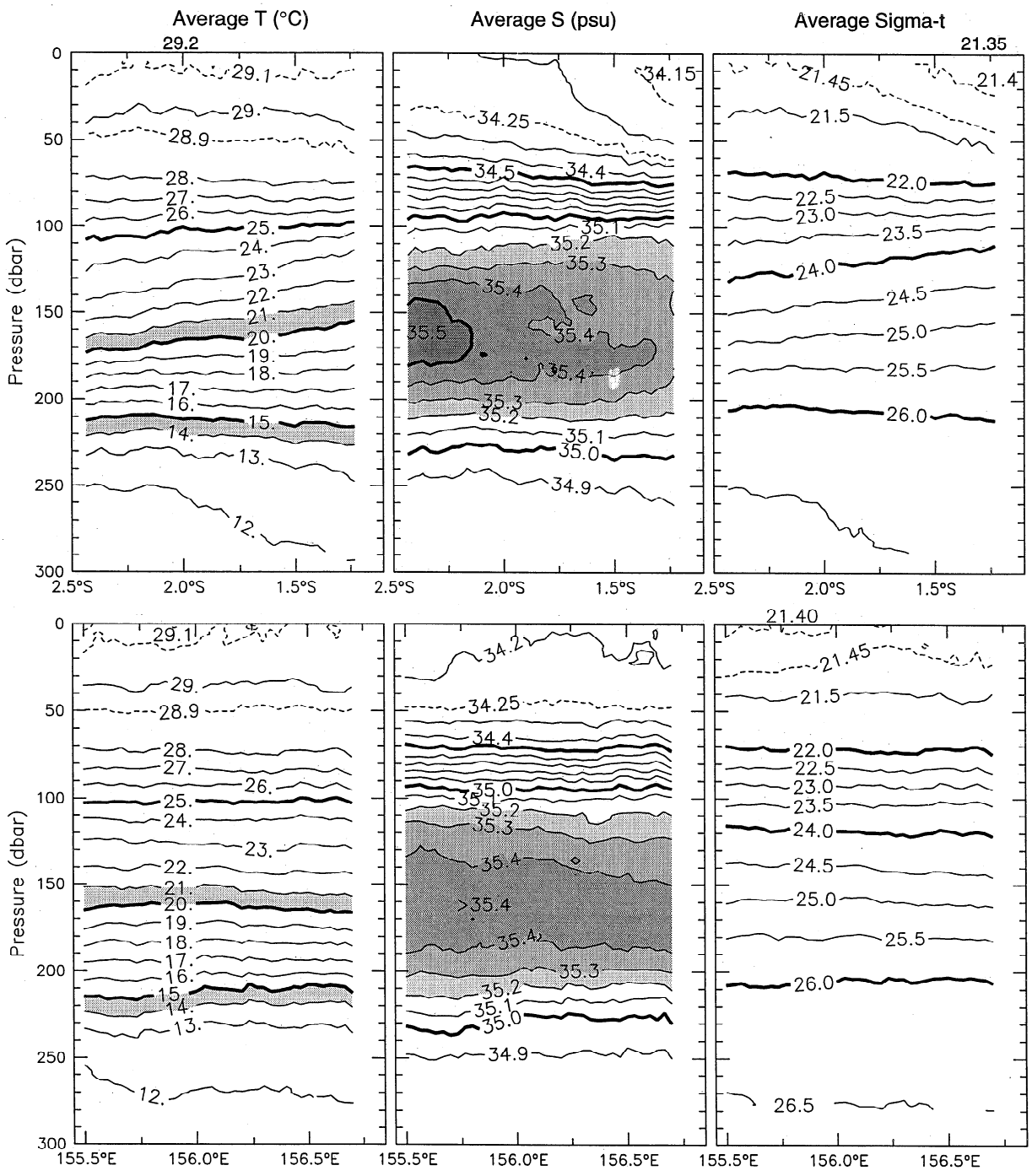

Figure 5. Distribution of time-averaged (left) temperature, (middle) salinity, and (right) sigma-t in the upper 300 m along (top) N2S and (bottom) W2E. These averages were calculated from the 2-dbar pressure-gridded values. Extra (dashed) contours show the structure in the low-gradient near-surface layer.

Intertropical Convergence Zone north of the equator, though surface salinities on the equator are sometimes raised by equatorial upwelling [*Toole et al.*, 1988]. Waters in the upper thermocline are warmer and lighter at SBS than at SBN, while waters in the lower thermocline are colder and denser at SBS than at SBN; these gradients are consistent with geostrophic shear above and below the core of the EUC. The salinity maximum is more intense (by 0.2 psu) and much less variable at SBS than SBN. The deep thermostad (250 to 300 m) is cooler (by 0.6°C) and slightly fresher (by 0.03 psu) in the south than in the north (Figure 4).

Vertical sections (Figures 5 and 6) show that meridional variations are generally monotonic with latitude, though the sign changes with depth. Zonal gradients are comparatively weak and generally insignificant. Within the upper 60 m, the average salinity decreases northward toward the equator, and the top of the halocline (at ~34.3 psu) slopes down toward the north. Within this surface layer, the average temperature has very weak stratification (<0.01°C m^{-1}) and no systematic meridional gradient. Within the thermocline, the 19°to 24°C isotherms slope up toward the equator, and the 12° to 13°C isotherms slope down toward the equator, while the 15° to 17°C isotherms are very nearly level. Isopycnals generally parallel the isotherms (Figure 5). Through geostrophy and the thermal wind relation, the average temperature and density sections suggest that the core of the EUC was near the 16°C isotherm, at a depth of about 200 m; this is consistent with the average distribution of currents measured by the ship's acoustic Doppler current profiler (Figure 7), which shows strongest eastward flow (>0.35 m s^{-1}) at a depth of ~175 m at the north end of our section.

The subsurface salinity maximum (S >35.3 psu) lies within the layer of upward sloping isotherms and isopycnals at depths between 120 and 200 m (Figures 5 and 6). Because of the vertical excursion of isopycnals, this feature appears to be less intense and thicker when sections are averaged on isobars (Figure 5) rather than isopycnals (Figure 6). The isopycnal averaging (Figure 6) shows the 35.5 psu isohaline extends through our zonal section, to as far north as 1.5°S. The intensity of the maximum decreases, while its variability increases

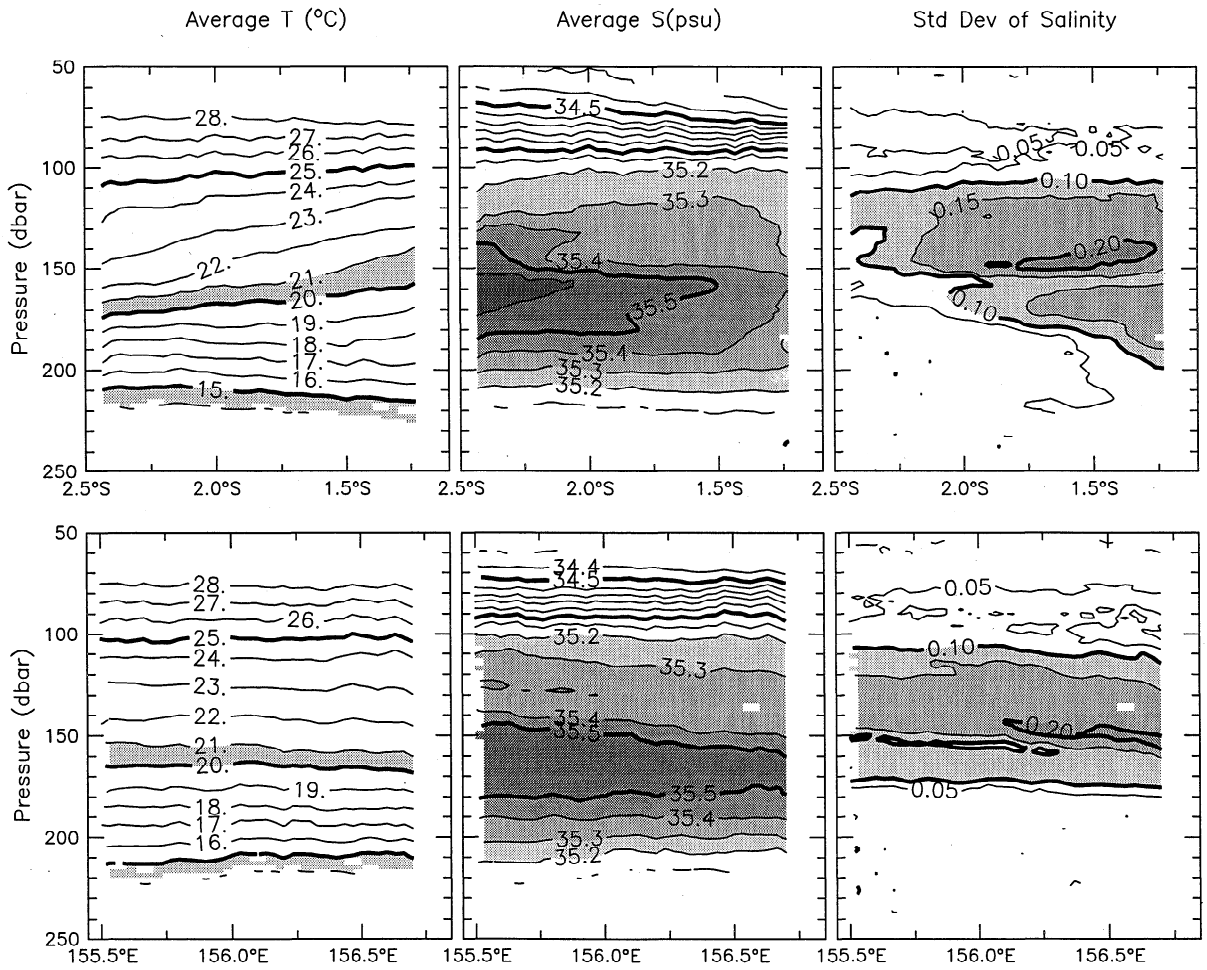

Figure 6. Distribution of time-averaged temperature and salinity within the thermocline, along (top) N2S and (bottom) W2E; the standard deviation of salinity along both lines is also shown. These statistics were calulated from the 0.1 kg m^{-1} density-gridded data and plotted versus the time-averaged pressure of each bin.

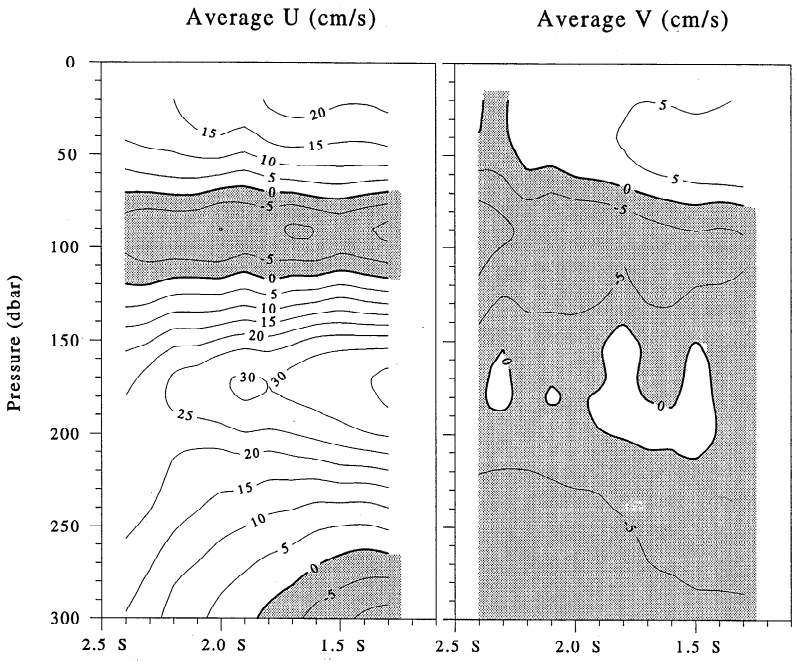

Figure 7. Distribution of the average zonal (U) and meridional (V) current along N2S, from ADCP on *Wecoma*. Shaded areas indicate westward or southward flow.

toward the north (Figure 6); the regions of maximum variability coincide roughly with regions of high vertical shear above and below the core of the EUC (Figures 6 and 7). The salinity maximum and the EUC core lie at about the same depth, but water carried by the EUC is less saline than water farther south because of upstream dilution with low-salinity North Pacific waters [*Tsuchiya et al.*, 1989].

4. Cruise-Averaged Sections

The very different local forcing regimes corresponding to the three survey periods can be characterized by their average wind stress, surface heat flux and precipitation values (Table 4): calm winds, low rainfall and net heating during the first survey period; strong westerly winds, high rainfall, and net cooling during the second; and moderate northwesterly winds, moderate rainfall, and no net heating or cooling during the third. To see whether these cruise-to-cruise weather differences were reflected in the upper ocean, temporal averages of the thermohaline fields were calculated separately for each cruise, using both the pressure-gridded data and the density-gridded data. Results (Figures 8, 9, and 10) are shown for the meridional section only, since cruise-averaged properties at all locations on the zonal section are similar to those near the midpoint of the meridional section.

Cruise-to-cruise differences in surface layer properties (Figures 8 and 9) are consistent with differences in the mean winds and surface fluxes (Table 4). Although the surface layer was very warm (>28.5°C) in all three survey periods, it was distinctly cooler (by ~0.3°C) during December 20 to January 9 (Figure 9), the survey period with strongest westerly winds and net heat loss (Table 4). The average temperature stratification in the upper 50 m was relatively strong (~0.04°C m^{-1}) during November 13 to December 2 (Figures 8 and 9), the survey period with calm winds and strongest surface heating (Table 4); it was nearly absent (<0.01°C m^{-1})

Table 4. Average and Standard Deviation of Daily Averaged Wind Stress (Positive Eastward or Northward), Precipitation, and Surface Heat Flux (Positive Upward), for Each Survey Period

	$< \tau_x >$, Pa	$< \tau_y >$, Pa	τ'_x, Pa	τ'_y, Pa	$< P >$, mm	P, mm	$< Q_T >$, W m^{-2}	Q'_T, W m^{-2}
Nov. 13 to Dec. 2	0.006	0.001	0.015	0.015	1.9	3.6	–66.3	64.4
Dec. 20 to Jan. 10	0.045	–0.035	0.048	0.032	12.3	17.6	14.6	77.8
Jan. 27 to Feb. 15	0.034	–0.027	0.022	0.013	4.5	7.8	–1.3	55.9

Wind stress data (provided by R. Weller) are from the Woods Hole Oceanographic Institution buoy at 1°45′S, 156°00′E. Rainfall and surface heat flux estimates (provided by C. A. Paulson) were obtained from measurements aboard *Wecoma* and do not include the heat flux by rainfall.

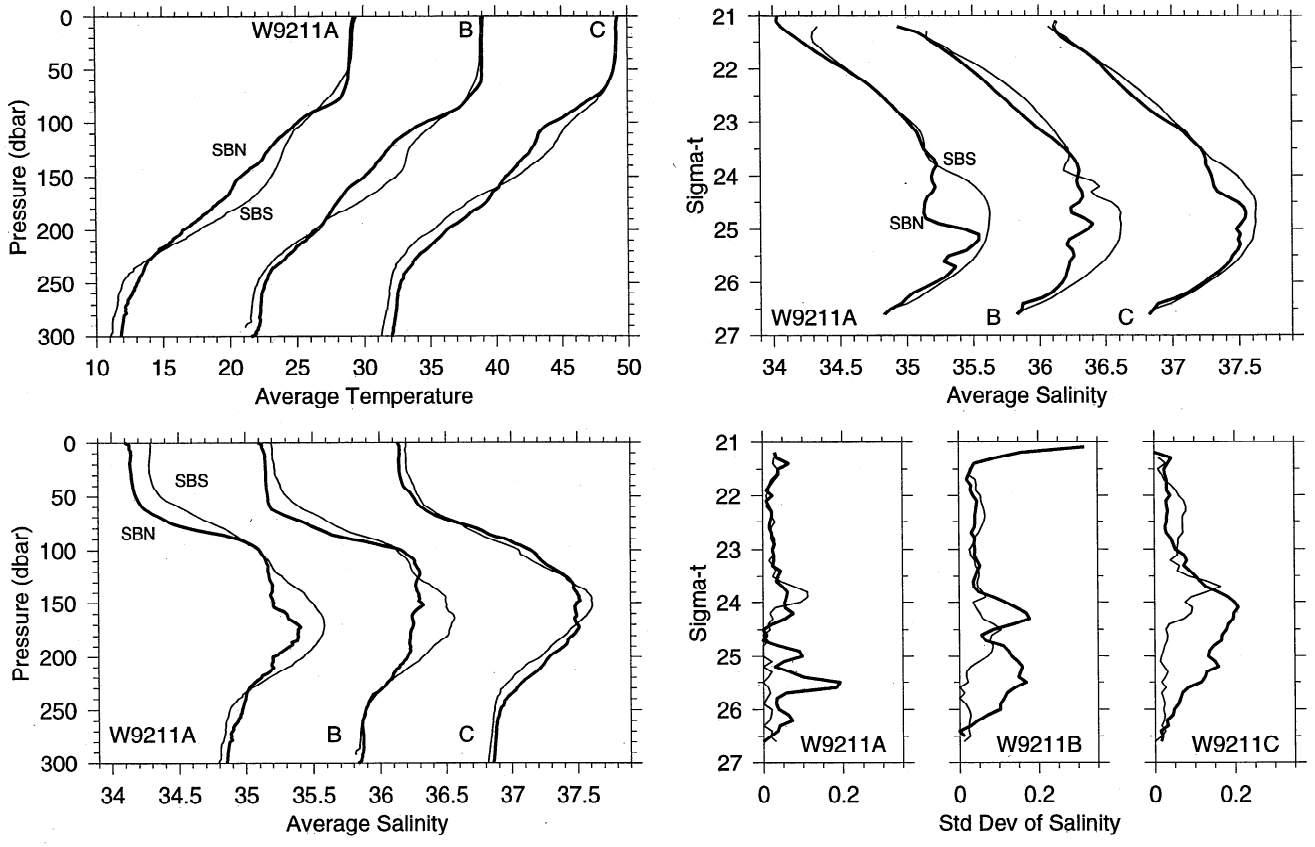

Figure 8. Vertical profiles of the cruise-averaged temperature and salinity near SBN (thick lines) and SBS (thin lines). Scales refer to profiles for W9211A; profiles are offset by 10°C or 1.0 psu for W9211B and by 20°C or 2.0 psu for W9211C. Profiles were calculated from both (left) pressure-gridded data and (right) density-gridded data.

during December 20 to January 9, the survey period with strong westerly winds and net surface cooling. In all three survey periods, the surface layer was very fresh (<34.3 psu) compared to the underlying thermocline waters, and near-surface salinities decreased toward the north end of the line (Figures 8 and 9); both are consistent with the absence of equatorial upwelling. The near-surface salinity stratification was stronger during the second survey period (Figure 9) when rainfall was high (Table 4). The zonal component of the near-surface currents was eastward during all three cruises (Figure 10) and was especially strong (>0.3 m s^{-1}) during the second survey period, when an eastward Yoshida jet developed in response to the local westerly winds [*Lukas et al.*, 1995a].

The thermocline remained at about the same depth (70 to 230 dbar) during the three survey periods (Figures 8 and Figure 11), except that the 13°C isotherm at the bottom of the thermocline at SBS was ~10 dbar shallower during the third period (Figures 8 and 11). The equatorward spreading of isotherms within the thermocline shoaled significantly between November and January: the horizontal isotherm changed from 15°C at 220 m during the first survey period to 17°C at 190 m during the second and 20°C at 160 m during the third (Figure 11). The meridional scale of this average isotherm spreading is of O(100 km); the depth of the sign reversal in the meridional temperature gradient shoaled from ~220 to ~160 dbar and warmed from ~14 to ~20°C (Figure 8). These changes and their scale are roughly consistent with the shoaling of the core of the EUC from ~190 to ~150 m (Figure 10). The average zonal velocity at the core of the EUC also intensified, particularly at the northern end of our N2S line, where it changed from about 0.25 m s^{-1} during the first survey period to >0.5 m s^{-1} during the third (Figure 10).

The structure and intensity of the subsurface salinity maximum also changed significantly (Figures 8 and 11). During all three cruises, the salinity maximum was most intense at SBS, the southern end of the N2S line. The depth of maximum salinity at SBS shoaled slightly (from 170 dbar during W9211A to about 145 dbar during W9211C, Figure 8) and lay within the layer of upward sloping isotherms ($\partial T/\partial y < 0$), just above the core of the EUC during all three survey periods. During the second survey, when the EUC was apparently centered at about 1.5° S (Figure 10), the structure of the high-salinity core was more complex, and the maximum salinity at SBN was lower (Figures 8 and 11). During the third survey period, the EUC core lay far-

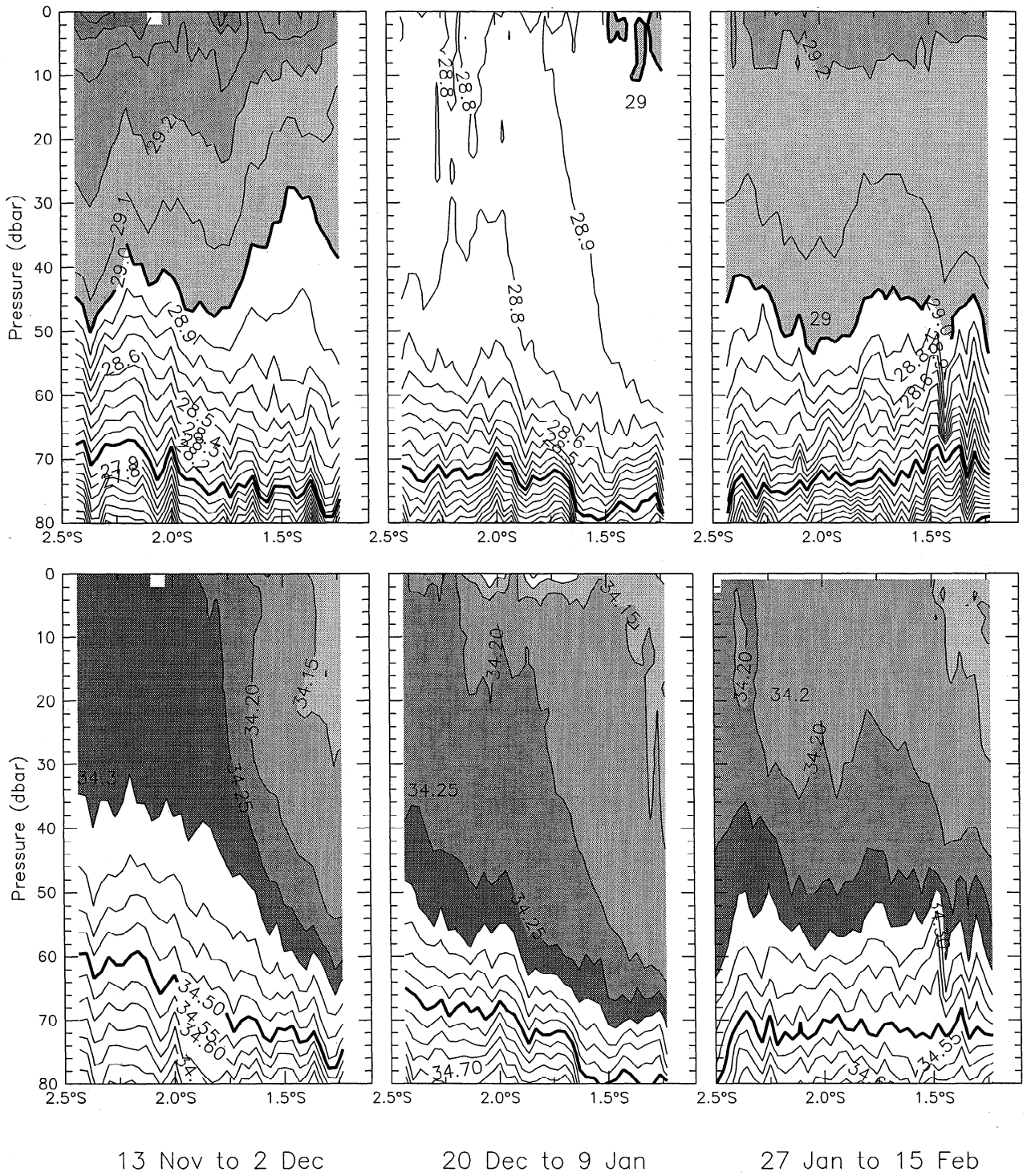

Figure 9. Distributions of the cruise-averaged near-surface (top) temperature and (bottom) salinity along the N2S line, calculated from the 2-dbar pressure-gridded values. Contour intervals are 0.1°C and 0.05 psu; areas with temperatures of 29.0°– 29.4°C or salinities of 34.25–34.30 are shaded.

ther north (Figure 10), and the intense salinity maximum layer extended along the entire length of the N2S section (Figure 11).

The most surprising result of comparing these cruise-averaged sections is that the core of EUC (represented by spreading isotherms and isopycnals) migrates across isotherms as well as in depth. Variations in the depth of the thermocline and in the strength and depth of the EUC have previously been observed in this region [*McPhaden et al.*, 1990, 1992; *McPhaden*, 1993] and can be explained in terms of a propagated response to remote forcing and large-scale pressure gradients

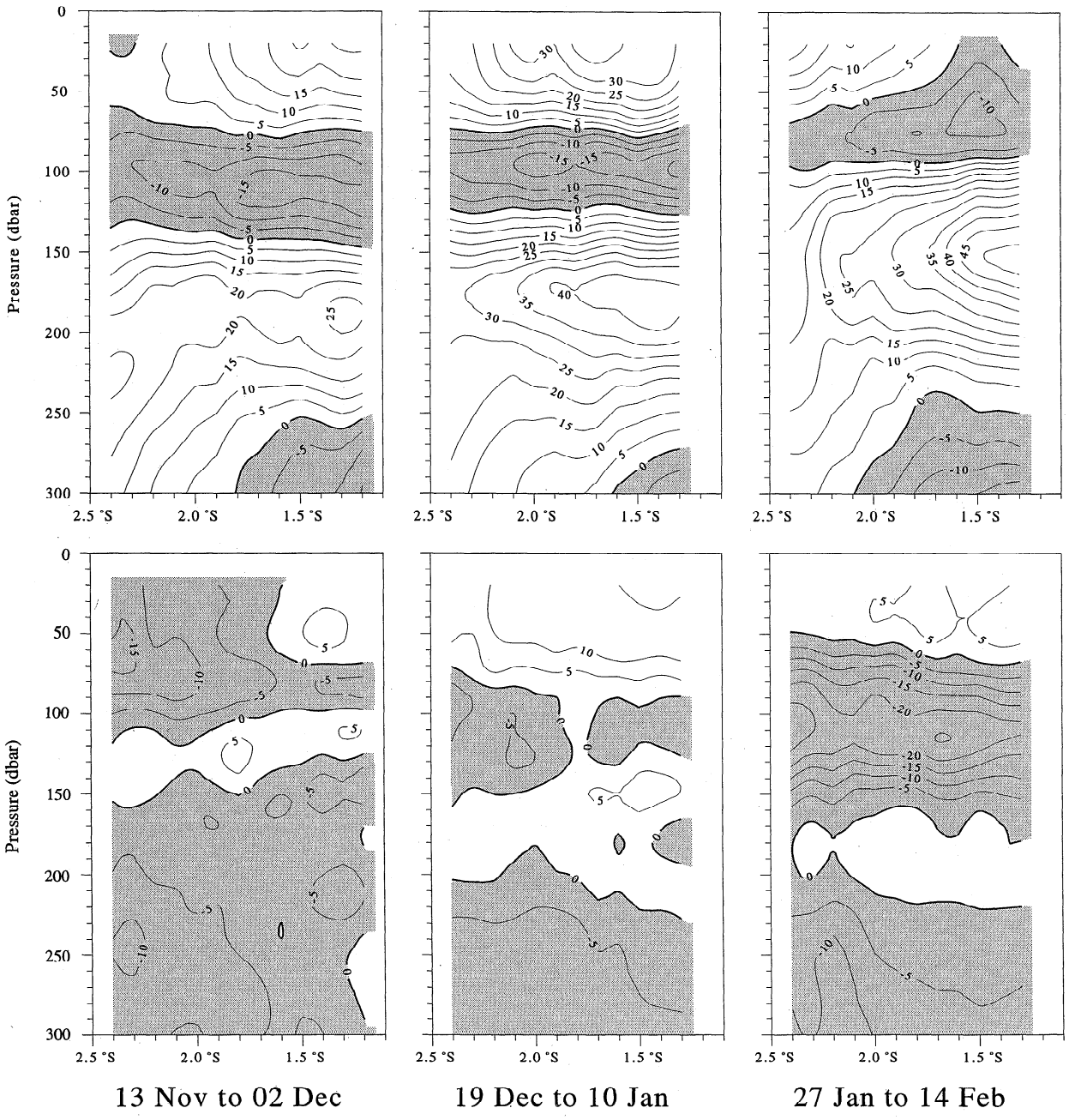

Figure 10. Distributions of the average (top) zonal and (bottom) meridional components of ADCP velocity along the N2S line, calculated separately for each cruise. Areas of negative values (westward or southward flow) are shaded.

[*McPhaden et al.*, 1990; *Kessler and McPhaden*, 1995]. We know of no dynamical models that include a mechanism for the EUC to migrate across isotherms.

5. Temporal Variability

A central purpose of the *Wecoma* surveys was to measure the temporal variability of the zonal and meridional structure on scales of 5–100 km during the COARE IOP. Since each occupation of the butterfly sampling pattern lasted about 32 hours, and the average repeat time was <2 days within each ~20-day survey period, our data can be used to study local variations on timescales of 2–20 days, as well as the spatial differences between cruises. Data from the moored array and stationary ships are more suitable for time series analysis, but these platforms provide very limited spatial information. Results from the moorings [*Weller and Anderson*, 1996; *Eriksen et al.*, 1995a, b; *Kutsuwada and Inaba*, 1995] and stationary ships [*Smyth et al.*, 1996a, b; *Wijesekera and Gregg*, 1996] show there is significant variability on both the long timescales (days to weeks) that can be resolved by the *Wecoma* sampling and on shorter timescales (<1.5 days) that were not resolved

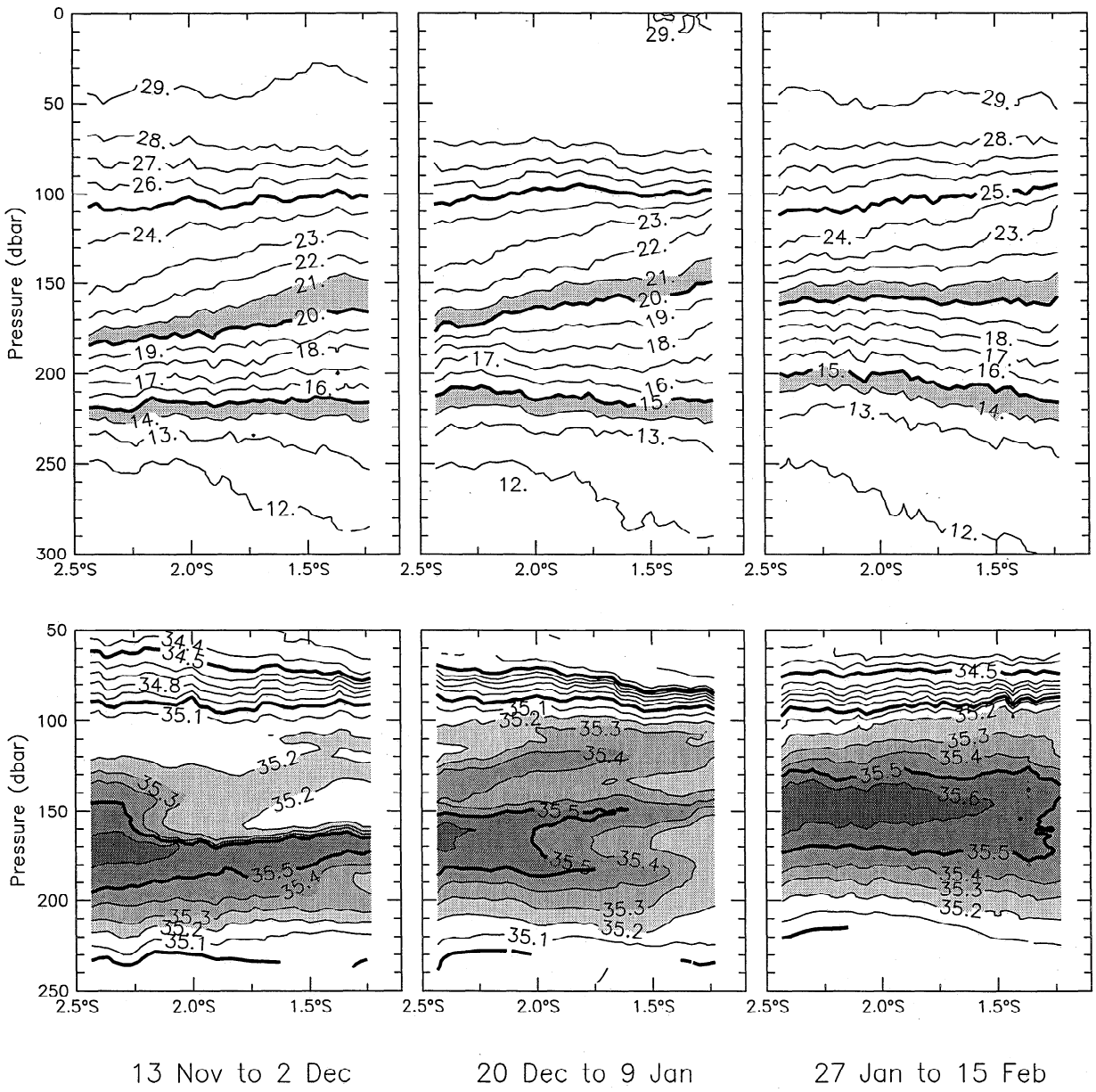

Figure 11. Distributions of cruise-averaged (top) temperature and (bottom) salinity along the N2S line, calculated from the 2-dbar pressure-gridded values (for temperature) and the 0.1 kg m^{-3} density-gridded values (for salinity).

in our sampling. Much of the high-frequency variability is due to semidiurnal internal waves and to diurnal cycling in the near-surface layers [*Moum and Caldwell,* 1994]; these and other high-frequency signals might appear as noise in our data. In this presentation of the temporal variability of the upper ocean in the COARE IFA, we include sampling time as an independent variable and use a variety of techniques to reduce the noise from high-frequency signals; these are described in the appropriate subsections.

5.1. The Near-Surface Layer

Water above the main pycnocline was usually well mixed or very weakly stratified (Figure 12, Plates 1 and 2) except in the upper 5–10 m, which sometimes showed evidence of surface heating or freshening, especially when winds were very weak (e.g., November 22, January 8) or following high rainfall (e.g., January 8). Rainfall that occurred during strong winds (e.g., December 20–25) caused slight freshening throughout the upper layer, to depths >40 m (Figure 12, Plate 2). Thermal stratification of the near-surface layer (Figure 12, Plate 1) was generally strong during W9211A (November 1992), when weak winds were prevalent. Salinity stratification of the near-surface layer was generally weak, under both weak and strong winds; strong salinity stratification in the upper 10 m was observed on only a few occasions (notably January 3–8) immediately following very heavy rainfall (Figure 12, Plate 2). The near-surface layer was well-mixed during portions

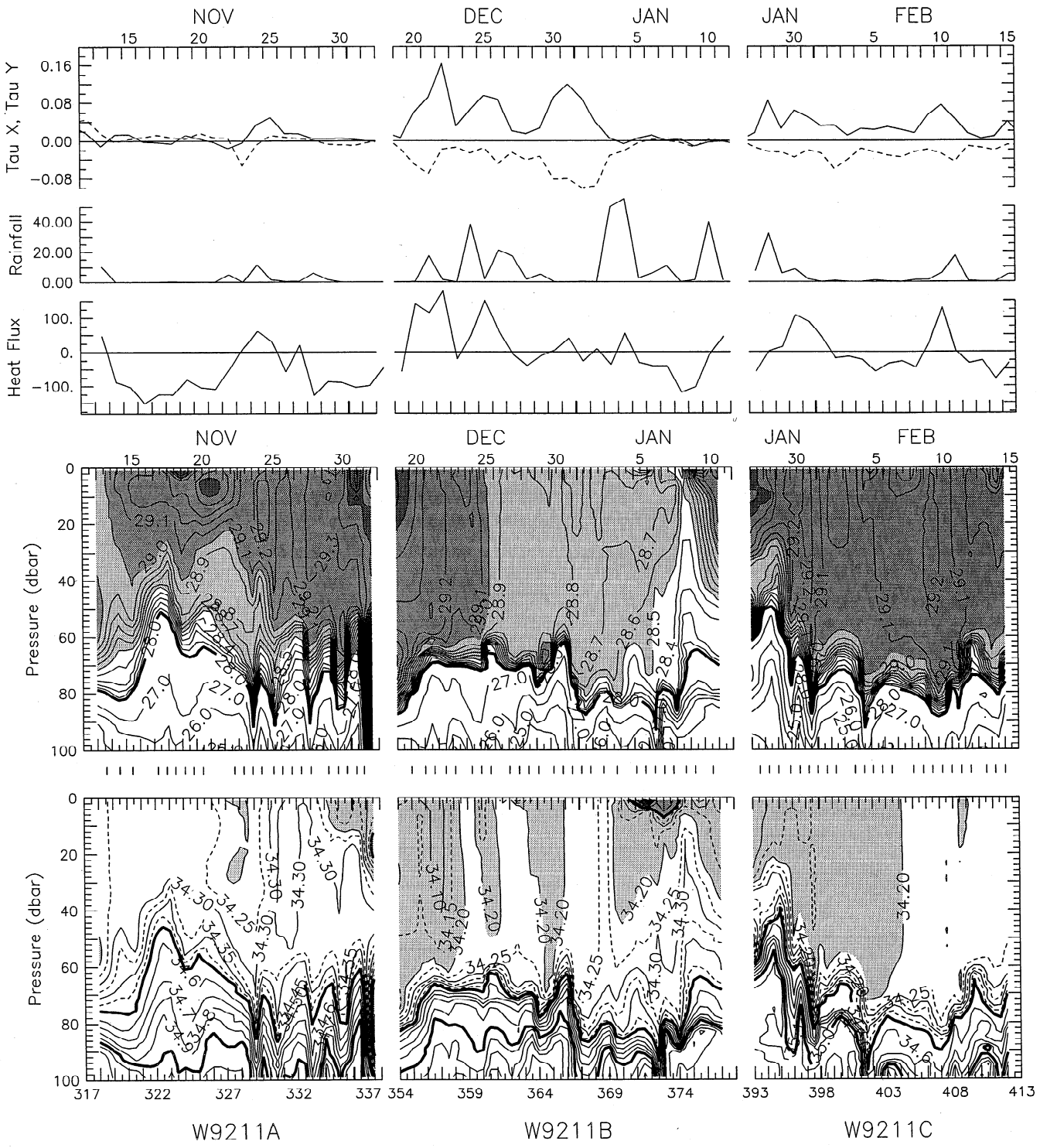

Figure 12. Time-depth distributions of upper layer temperature (middle panel) and salinity (bottom panel) at 1°50′S, 156°06′E; vertical tics between panels indicate the time of Seasoar profiles at this location. Daily averaged wind stress components (newtons per square meter, measured on IMET buoy), rainfall (millimeters per day, measured on *Wecoma*) and surface heat flux (watts per square meter, calculated from observations on *Wecoma*) are shown in the top panel. Contour intervals are 0.1°C at T >28°C, 1°C at T <28°C, 0.05 psu at S <34.5, and 0.1 psu for S >34.5.

of W9211B (late December) and W9211C (early February) when strong or moderate westerly winds prevailed.

Water properties at a depth of 20 dbar seem to be typical of the upper layer and relatively free of diurnal and tidal variations (Figure 12, Plates 1 and 2). We therefore chose the 20-dbar surface to examine the time-varying horizontal structure of the near-surface layer. Time-latitude and time-longitude plots of the 20-

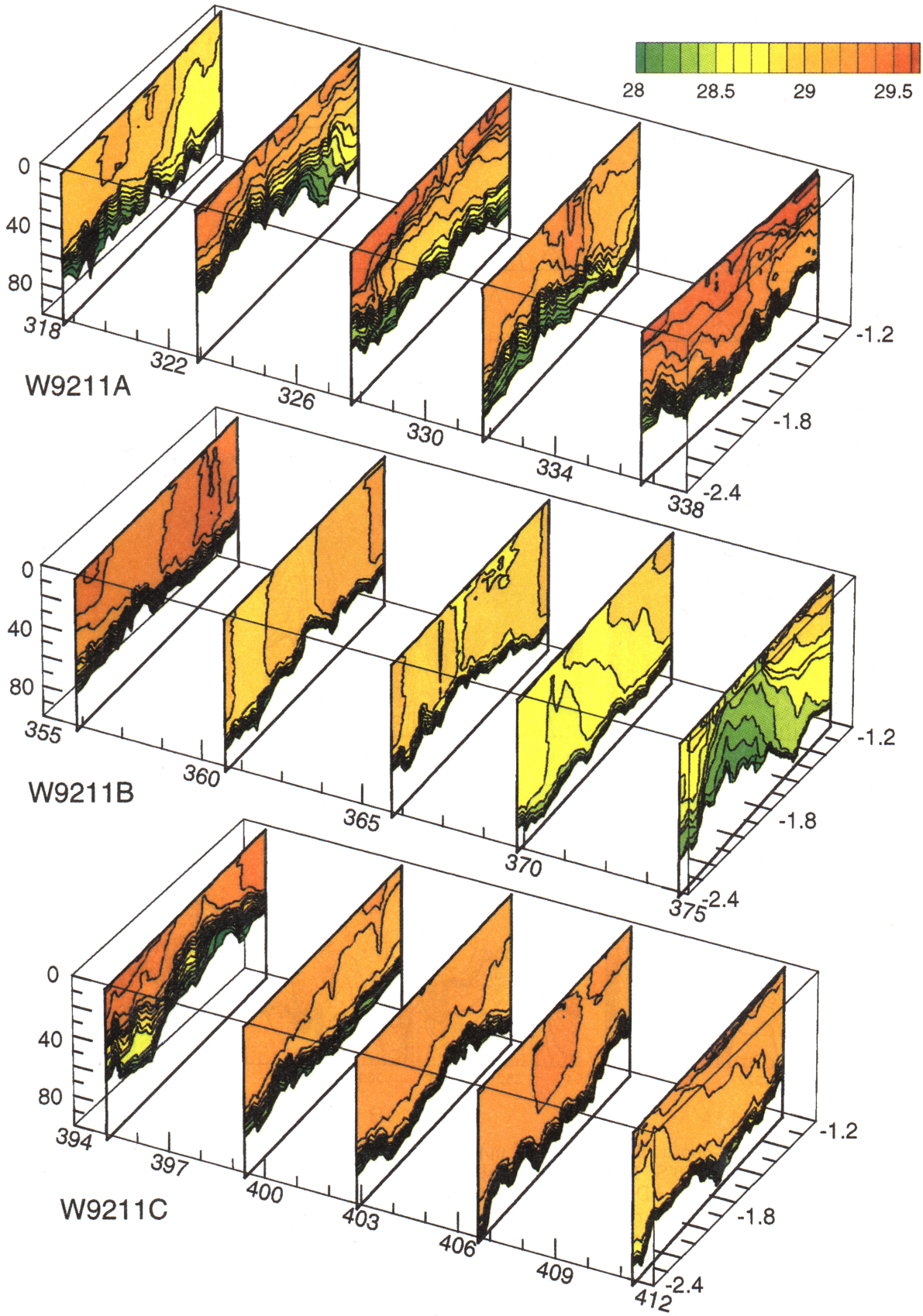

Plate 1. Time variation of upper layer temperature along 156°06′E during the COARE IOP, represented by a subset of N2S sections from each cruise (Table 2). Contours of T <28°C are suppressed. Time axis is labeled in day number, with day 367 corresponding to January 1, 1993. The sections shown begin on November 13, 17, 22, and 26; on December 1, 20, 25 and 30; on January 3, 8 and 28; and on February 2, 5, 9 and 14.

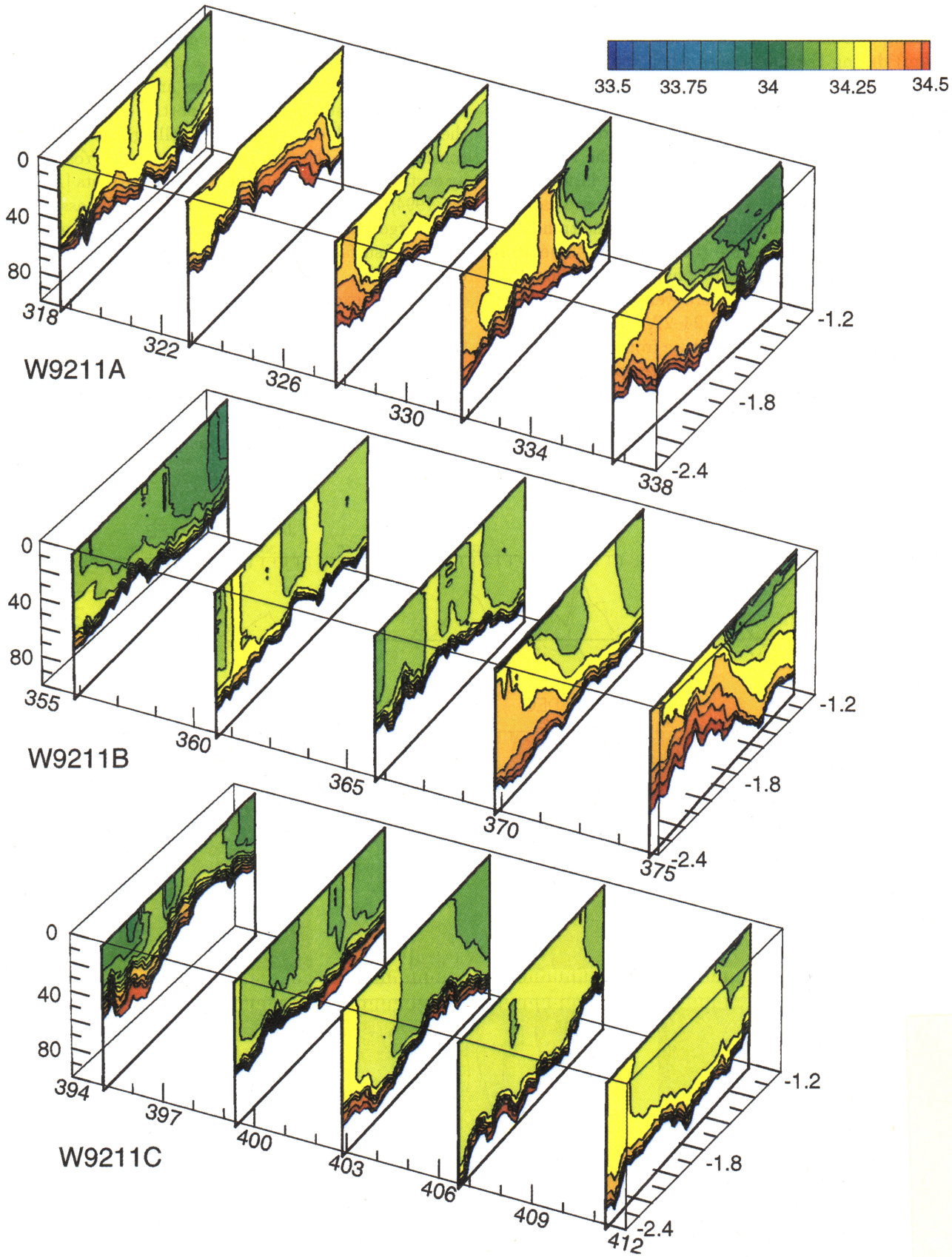

Plate 2. Time variation of upper layer salinity along 156°06′E during the COARE IOP, represented by a subset of N2S sections from each cruise. Contours of S >34.5 psu are suppressed. Time axis is labeled in day number, with day 367 corresponding to January 1, 1993. The sections shown begin on November 13, 17, 22, and 26; on December 1, 20, 25, and 30; on January 3, 8 and 28; and on February 2, 5, 9 and 14.

m temperature and salinity (Figure 13) show a general warming and increase in patchiness (at scales of ~10–30 km) during the first cruise when winds were weak, and show general cooling and homogenization during the strong westerly winds of the second cruise; the moderate winds of the third cruise similarly reduce patchiness. These trends are more obvious in the time series of the spatial averages and standard deviations (Figure 14); the meridional and zonal averages are indistinguishable, and they are subject to the same trends.

In general, the large-scale (50–100 km) temperature gradients were weak in both zonal and meridional directions (Figure 13a), but there were some notable exceptions. During December 24–27, while winds were strong and westerly, a temperature front (28.5°to 29°C) migrated 100 km northward. This temperature change occurred simultaneously along the entire W2E line, suggesting that a zonal front moved northward as a result of equatorward Ekman transport and equatorial downwelling driven by the strong westerly winds. The frontal migration rate (~0.3 m s^{-1}) is consistent with the Ekman transport estimate ($\tau_x/f = 1.5 \times 10^4$ kg m^{-1} s^{-1}, where τ_x is the zonal wind stress and f is the Coriolis parameter), assuming the transport is distributed over the top 60 m. Such a rapid downwelling response is also consistent with the rapid formation of the Yoshida jet by eastward acceleration of equatorial currents [*Eldin et al.*, 1994]. This migrating front seems to be associated with large residual cooling in a one-dimensional heat budget of surface layers at the center of the IFA [*Smyth et al.*, 1996b].

A second exception to the generally weak temperature gradients was observed in early January, soon after the end of the strong westerly wind burst (Figure 13a). A small local temperature minimum (T <28.5°C, diameter ~40 km) migrated 50 km northward along the southern half of the N2S line during January 5-8 and crossed the W2E line on January 9. This local tem-

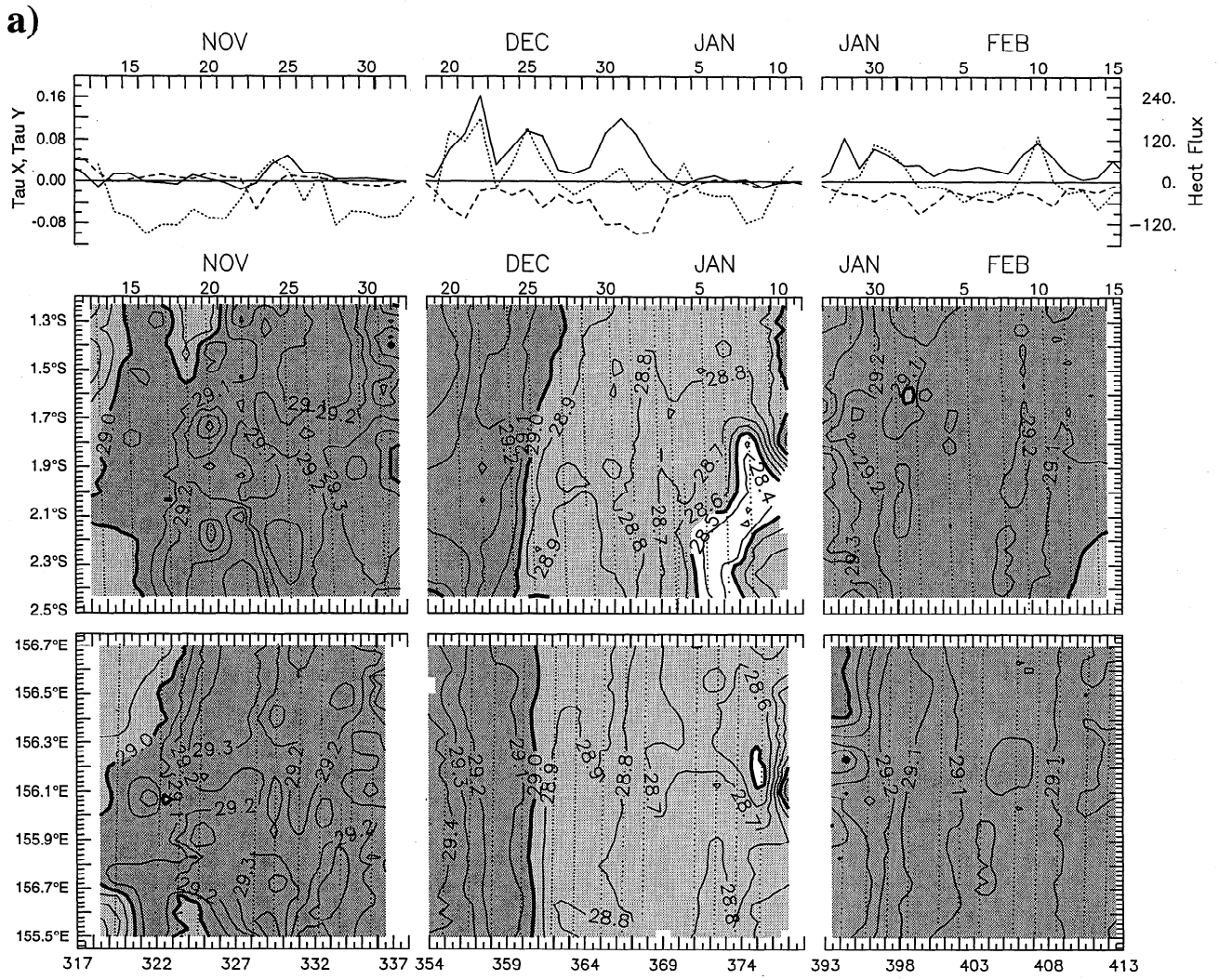

Figure 13. Latitude-time and longitude-time distributions of properties of the near-surface layer with time series of daily wind stress: (a) temperature at 20 dbar; (b) salinity at 20 dbar. Plots were made from individual 1-Hz ascending profiles (indicated by dots), interpolated vertically to 20 dbar.

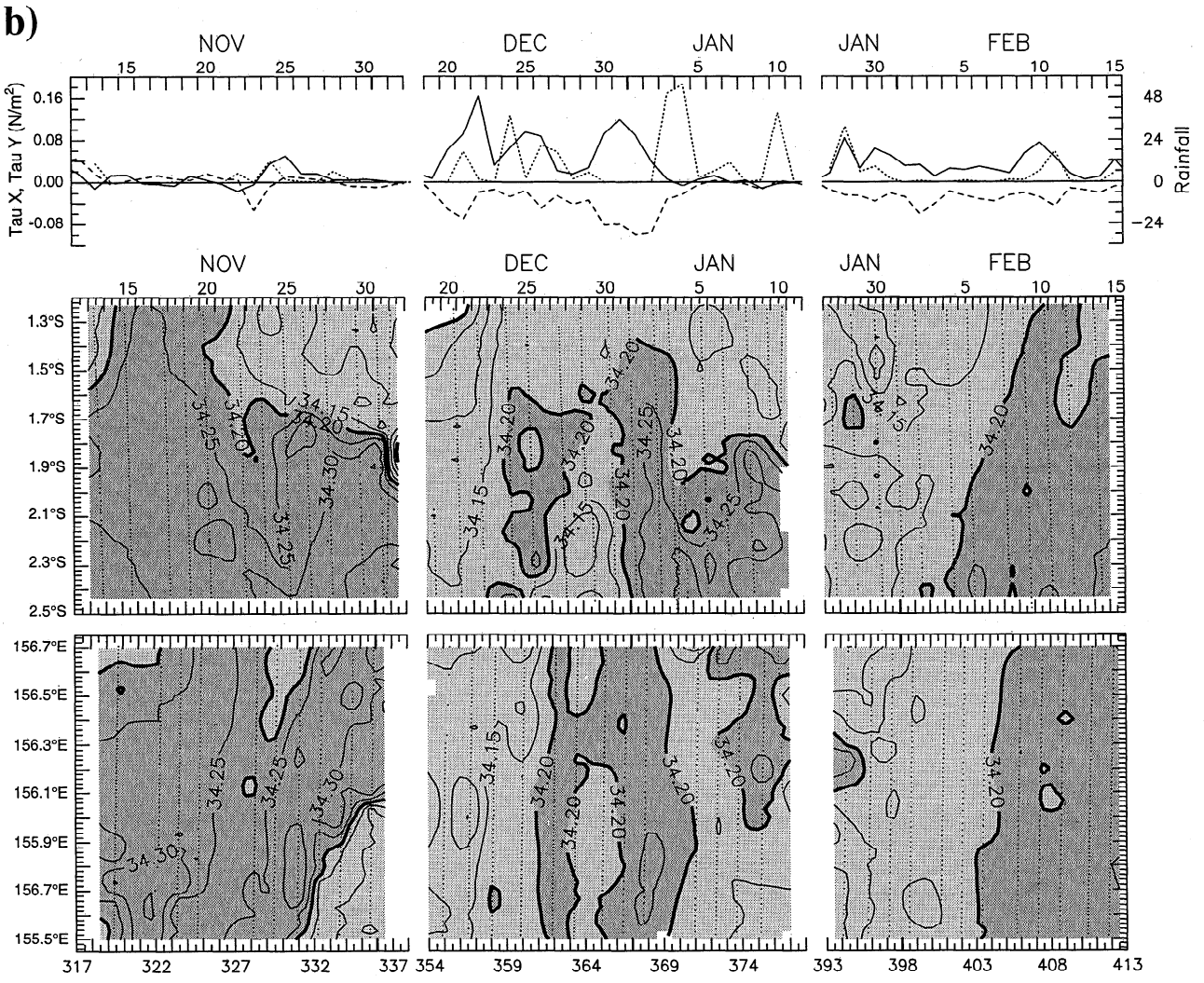

Figure 13. (continued)

perature minimum was connected to the bottom of the mixed layer, rather than to the sea surface (Figure 12); it could result from local upwelling or perhaps from mixing by high-velocity shear at the base of the mixed layer. Velocity data from a stationary ship adjacent to the IMET mooring [*Smyth et al.*, 1996a,b] and from the IMET and ADCP moorings [*Plueddemann and Weller*, 1994; *Kaneko et al.*, 1993] indicate this cold feature was on the southern flank of the decaying eastward jet [*Lukas and Hacker*, 1995]. Like the migrating front, this mesoscale feature seems to result in a strong cooling episode at the center of the IFA [*Smyth et al.*, 1996b].

The near-surface salinity field (Figure 13b) was less patchy than temperature (Figure 13a), and it had a persistent large-scale (50–100 km) meridional gradient, with lower values farther north. A rather sharp salinity front (at ~34.2 psu) migrated north-northeastward during November 13–15 and east-southeastward during November 25–30. Northward propagating isohalines were also observed during December 20–25 and February 4–10. Northward migration seems to associated with westerly winds which induce equatorward Ekman transport.

There was little or no correlation between the time-space fields of near-surface temperature and salinity (Figures 13a and 13b). For example, the two mesoscale features that were so obvious in the temperature field (i.e., the migrating front seen December 24–27 and the cold spot seen January 5–10) had no signature in the salinity field. Hence, each of the mesoscale features seen in either temperature or salinity is also reflected in the density.

5.2. The Thermocline

The near-equatorial thermocline is complex, and its different aspects (e.g., depth, thickness) can vary independently. In this section we describe variations in isotherm depth, thermocline thickness, strength of the vertical gradients, isotherm spreading, and temperature-salinity characteristics.

In the COARE IFA, the main thermocline coincides with a strong pycnocline (Figure 4), and this pycno-

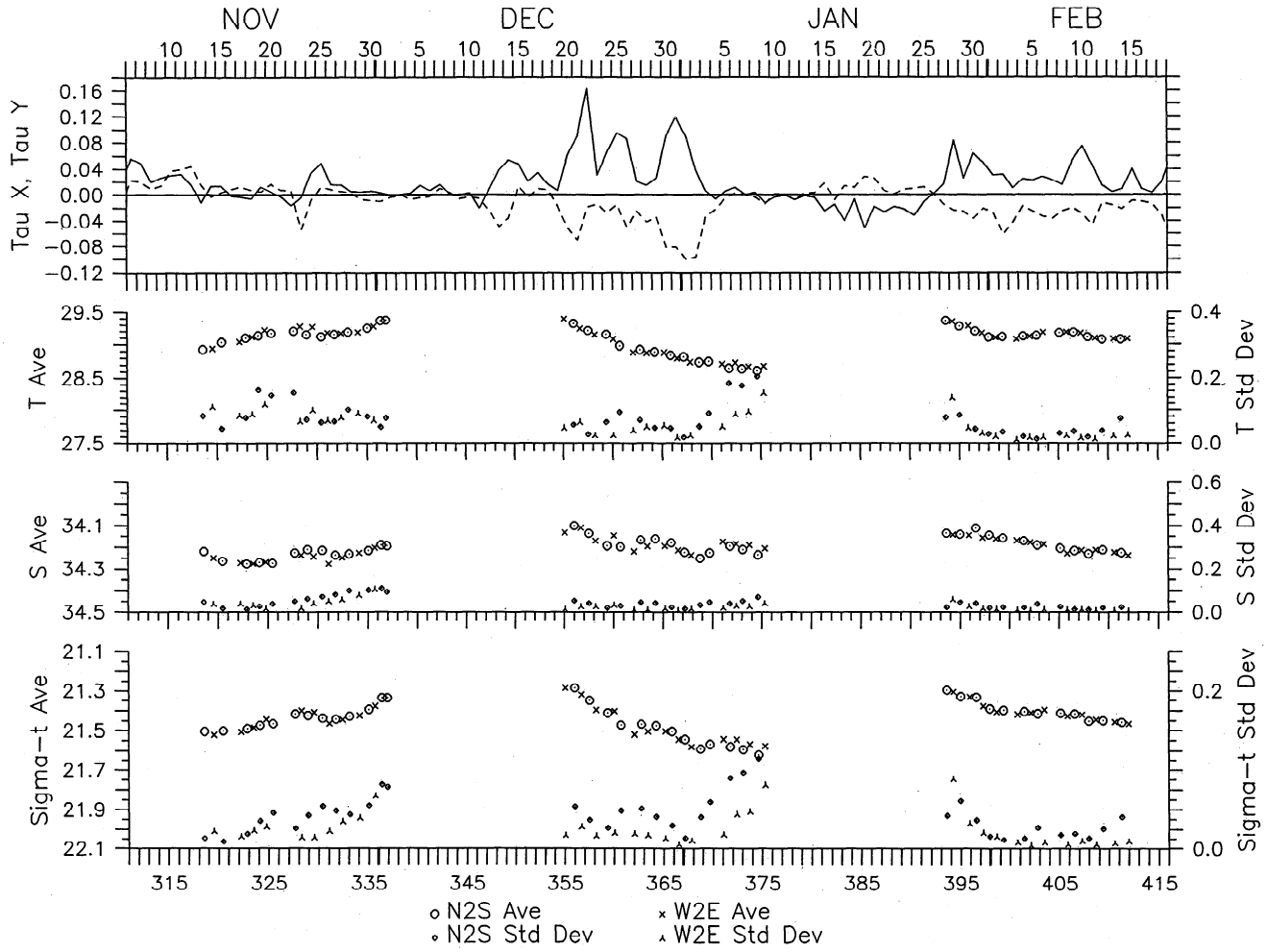

Figure 14. Time series of the spatial averages and standard deviations of 20-dbar temperature, salinity, and density anomaly (sigma-t) along the N2S and W2E lines, with time series of wind stress components in the top panel. Statistics were calculated from the 2-dbar, 2-nm gridded data.

cline (with σ_t of $\sim$ 22–26 kg m^{-3}) lay in the depth range of about 80–200 m throughout the COARE IOP Figure 15). Temperature varied nearly monotonically with density, with only a few small inversions (Figure 15). The 28°, 20°and 14°C isotherms, lay near the top, middle, and bottom of the thermocline (Figures 5 and 11) respectively, and coincide approximately with the 22.1, 25.2, and 26.2 kg m^{-3} isopycnals (Figure 15); the 23°C isotherm lay in the upper thermocline near the 24.2 kg m^{-3} isopycnal. The depths of some isotherms varied with latitude as well as in time Figure 16, and the various isotherms do not behave in unison.

The 28°C isotherm near the top of the thermocline was relatively deep (>70 m) during and immediately after westerly winds (Figure 16), and it was shallowest ($\sim$5 m) after the period of sustained easterlies lasting from January 7 to 26. These easterly winds were quite weak at the center of the IFA, but the TOGA-Tropical Atmosphere Ocean (TAO) Atlas moorings at 2°N, 156°E, and 0°N, 157.5°E [*McPhaden,* 1995; *N. Soreide*, personal communication, 1994] and the shipboard observations from Noroit [*Eldin et al.,* 1994] show they covered a large area and were stronger on and north of the equator. The resulting equatorial upwelling apparently caused uplift of the upper thermocline as far south as 2.5°S, i.e., along the entire N2S line. After the resumption of moderate westerly winds and equatorial downwelling (on January 26), the 28°C isotherm dropped rapidly to a depth of about 80 m and remained constant through the remainder of the third survey period.

Within the main thermocline there were subtle and complex variations in isotherm depth (Figure 16). The vertical coherence varied from one survey period to the next and within survey periods. For example, the depths of the 20°and 23°C isotherms were in phase during November and late December but out of phase in mid-February (Figure 16). In late December and early January, temporal changes in the depth of the 14°C isotherm seem to mirror those of 23°C isotherm, particularly at the northern end of our sampling pattern (Figure 16).

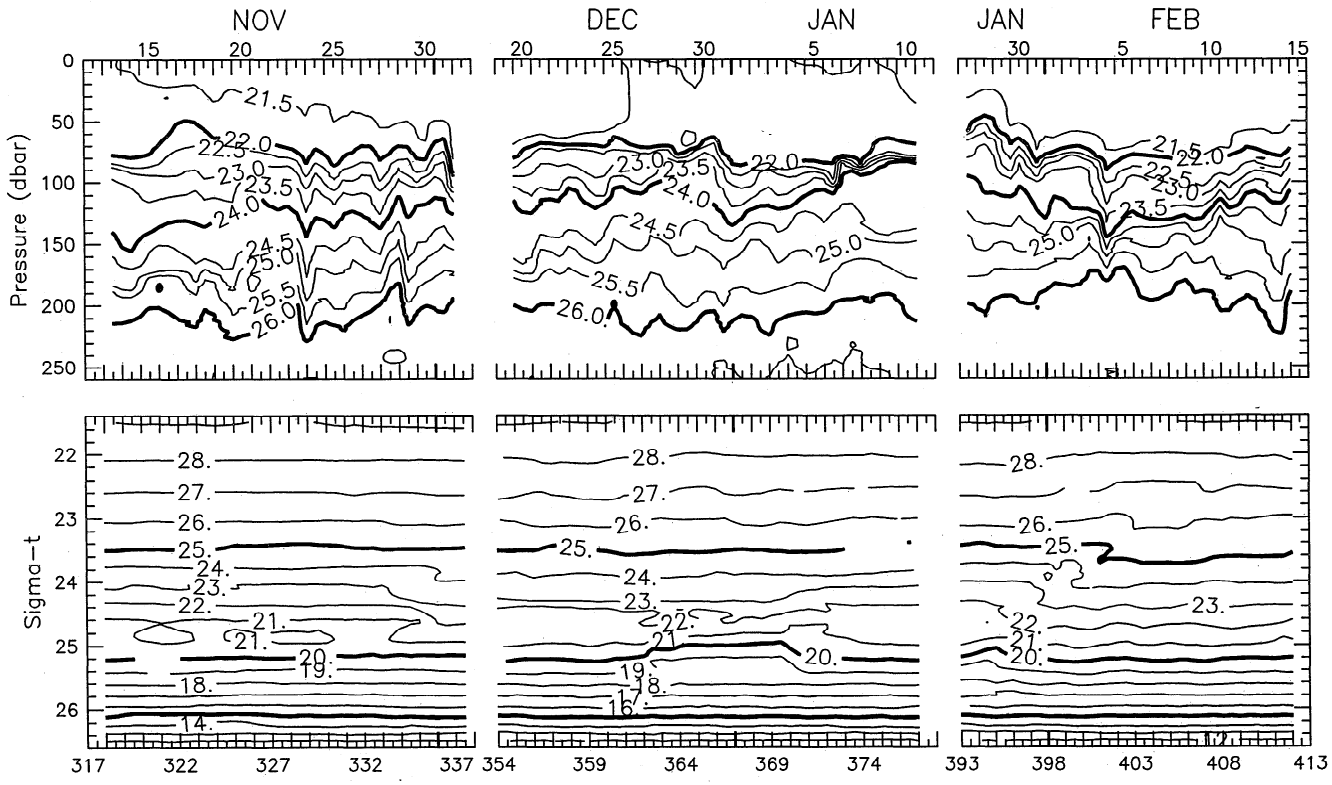

Figure 15. Time-depth distribution of (top) density and (bottom) time-density distribution of temperature at the intersection (1°50′S, 156°06′E), contoured from ascending 1-Hz data; sampling times are indicated by the tics between (top) and (bottom) panels. Contour intervals are 0.5 kg m^{-3} and 1°C, with heavy contours at intervals of 2 kg m^{-3} and 5°C.

The main thermocline was typically about 140 m thick (Figures 15 and 16), but this thickness varied, from more than 160 m in November to less than 120 m in early February.

A surprising feature of the time-depth distribution of density (Figure 15) is the growth and disappearance of weakly stratified layers within the main pycnocline. During much of the first survey period, the vertical density gradient $\partial\rho/\partial z$ has a rather small range ($\partial\rho/\partial z = 0.02$ to 0.05 kg m^{-4}, or $N = 5$ to 10 cph). A more nearly uniform layer (with $\partial\rho/\partial z < 0.02$ kg m^{-4}, $N < 9$ cph) occurred at σ_t of 24.0–24.5 kg m^{-3} through most of November, December 20–30 and January 6–10. Another weakly stratified layer occurred at 25.0–25.5 σ_t from November 20 to 27 and from December 25 to January 4. Strongly stratified layers were also ephemeral, and occurred at the top of the pycnocline (i.e., the bottom of the surface mixed layer); strongest stratification (N >20 cph) occurred during January 5–10 .

Latitudinal tilting of isotherms within the thermocline varied with both depth and time. The upper thermocline (represented by 23°C) sloped up to the north throughout the entire IOP, though the slope varied from $< 2 \times 10^{-4}$ to $> 4 \times 10^{-4}$ (Figure 16). The midthermocline (20°C) also sloped up to the north in November, December, and early January but had no significant slope in February. The lower thermocline (14°C) had no significant tilt in November but sloped down to the north in December, January, and February (Figure 16). These slow variations in isothermal tilts seem to be related to the zonal currents: the eastward surface current (above ~28°C and ~70 m), the westward flow at the top of the thermocline (~23–28°C and ~70–120 m), and the eastward EUC (~13–24°C and ~120–250 m) all accelerated during the westerly wind burst [*Lukas et al.*, 1995a]. The core of the EUC lay between the 14°and 23°C isotherms (compare Figures 10 and 11), and the thickness of this layer increased with latitude toward the equator (Figure 17).

Water mass characteristics of the thermocline vary in complex ways. Temperature-salinity characteristics tend to be simplest at the southern end of our sampling pattern, where there was almost no temporal variability in water characteristics below the 20°C isotherm (Figure 18). Farther north, there is a wide range of T-S characteristics in the density range of 23.5 to 25.5 kg m^{-3}. Within this range, there is a general tendency for waters to be cooler and fresher farther north than waters on the same isopycnal farther south.

5.3. Salinity Maximum

Water mass variations can be seen most clearly in the structure of the salinity maximum embedded in the lower thermocline (Figure 18 and Figure 19). This

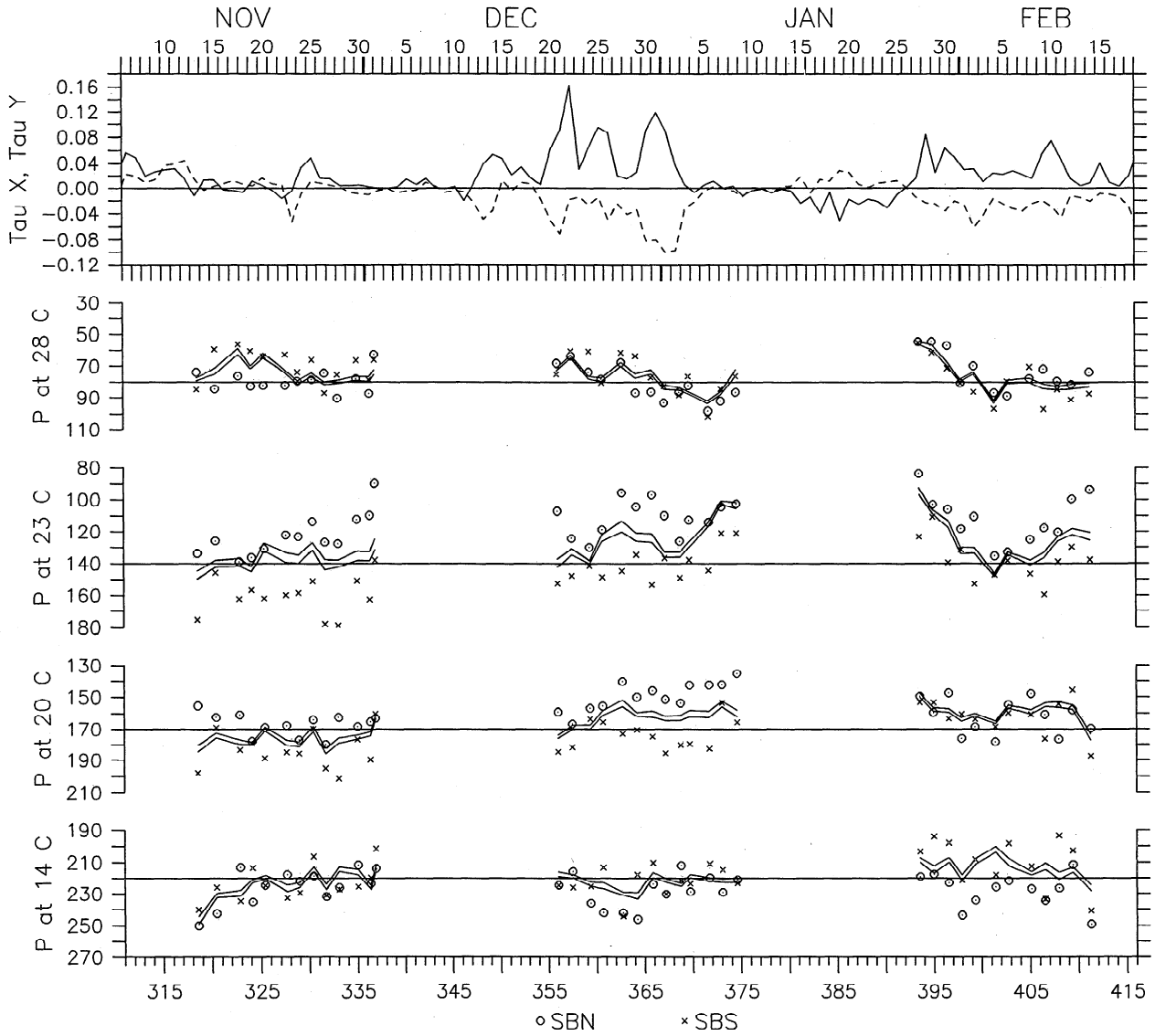

Figure 16. Time series of the depths of selected isotherms: at the southern (crosses) and northern (circles) ends of the N2S line and averaged along the N2S line (shown as lines plotted 1 standard error above and below the mean); time series of average isotherm depths along the W2E line are similar.

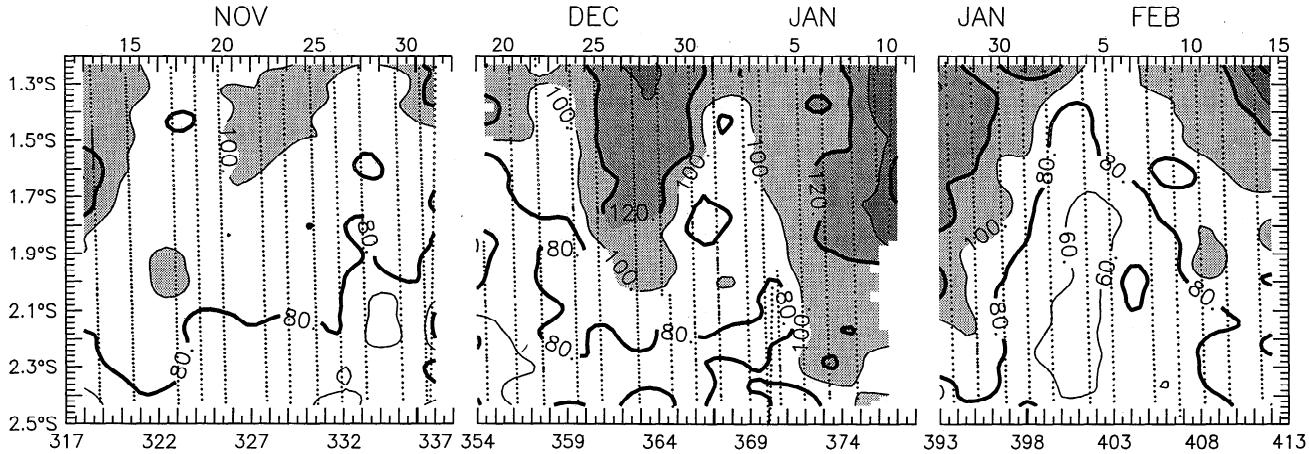

Figure 17. Latitude-time distributions of the thickness of the layer between the 23°C and 14°C isotherms, smoothed with half power at 5 days and 20 km.

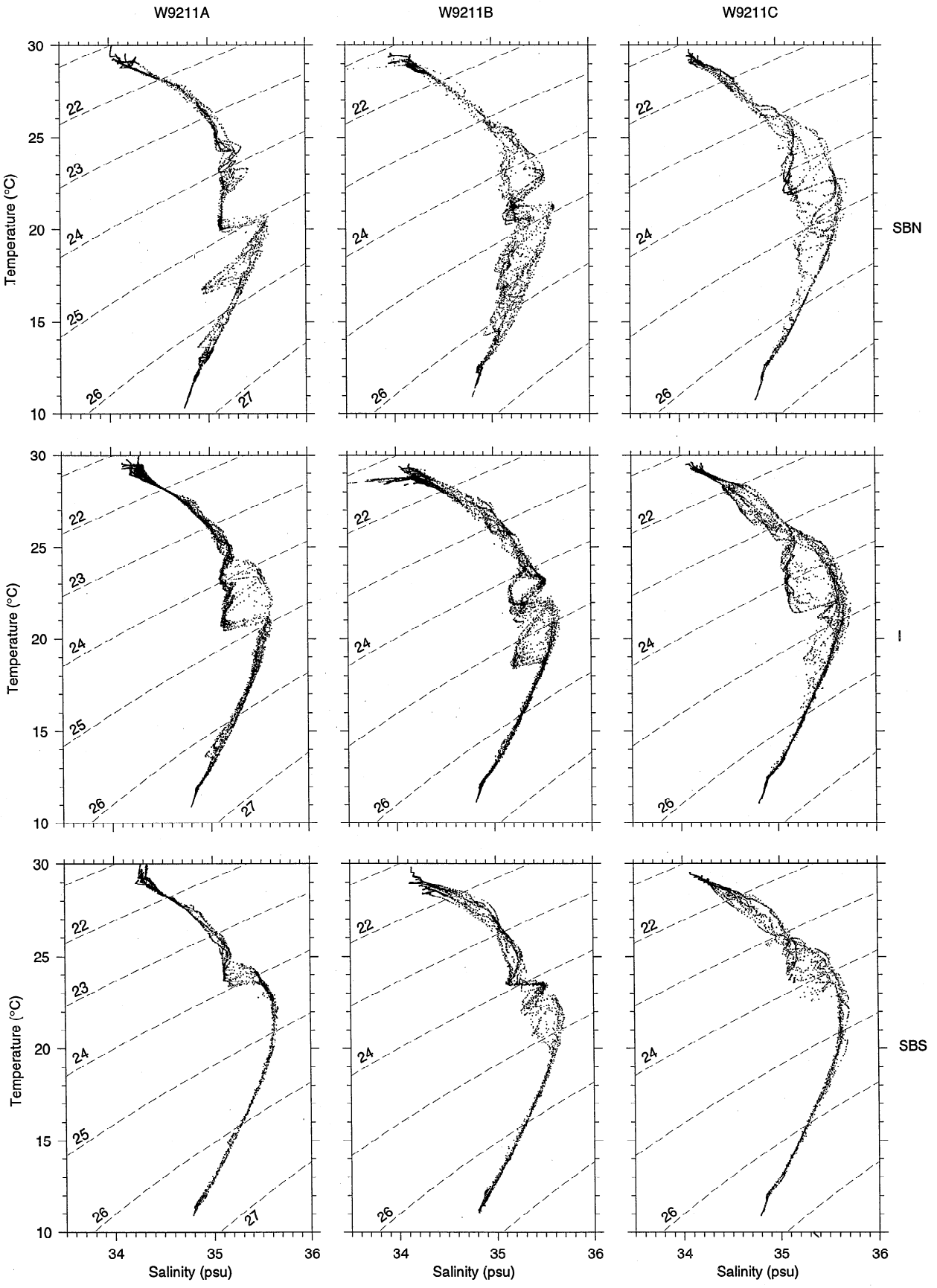

Figure 18. T-S characteristics at (top) the north end (SBN), (middle) the midpoint (I), and (bottom) the southern end (SBS) of the N2S line, for each survey period.

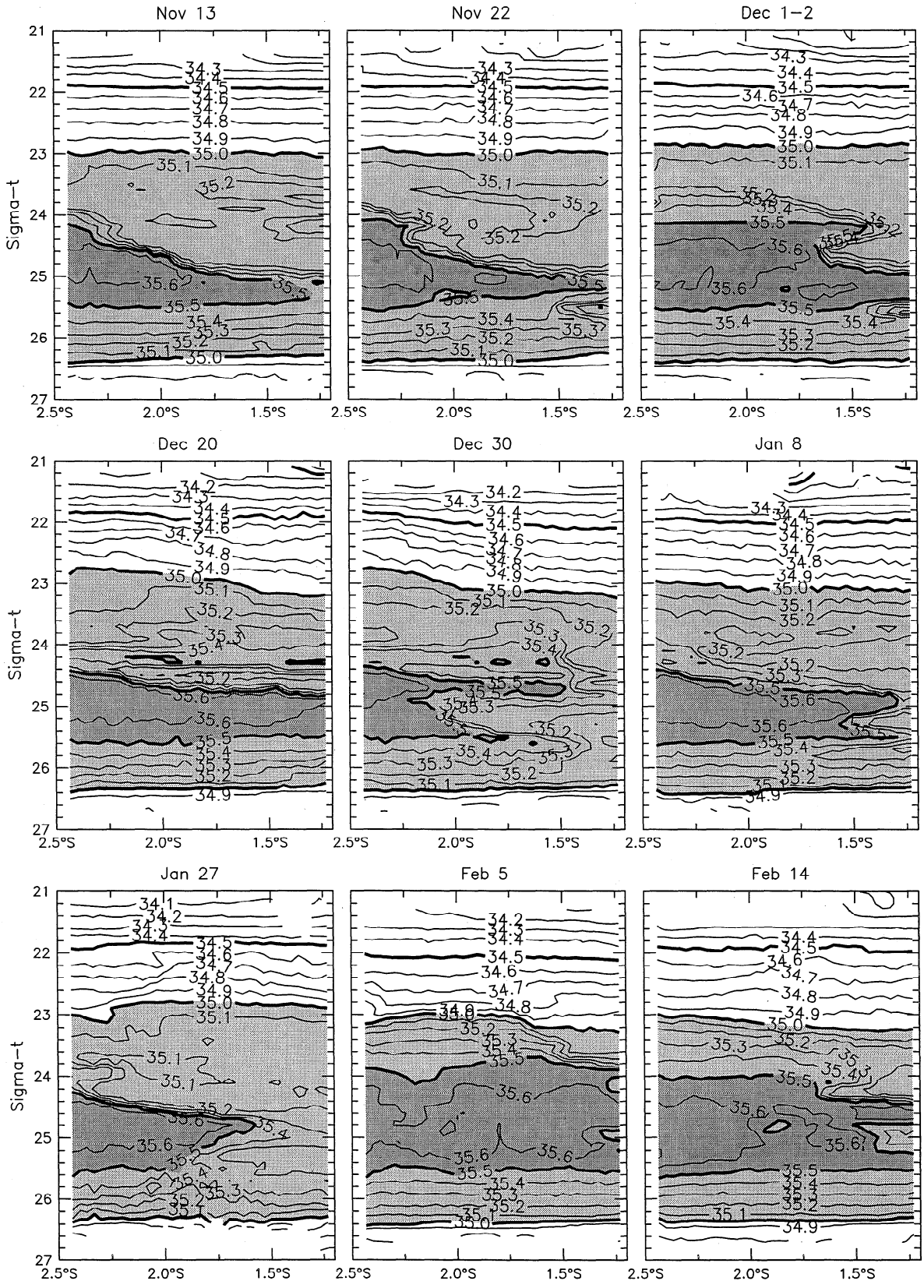

Figure 19. Salinity distributions along the N2S line, at the beginning, middle, and end of the each cruise, with density rather than depth as the vertical axis to remove fluctuations due to internal waves.

broad tongue of high-salinity water extends northward across the equator (Figure 2) from the South Pacific Ocean [*Tsuchiya et al.*, 1989; *Richards and Pollard*, 1991], though mean meridional velocities at that depth are small (Figures 7 and 10). Both the shape and the intensity of the high-salinity core varied during the COARE IOP. A subset of individual sections from the beginning, middle, and end of each cruise suggests that the larger structure (with meridional scales >50 km and density range >0.5 kg m^{-3}) tends to persist for at least 10 days but that smaller or thinner features have shorter timescales. For example, the main tongue of the

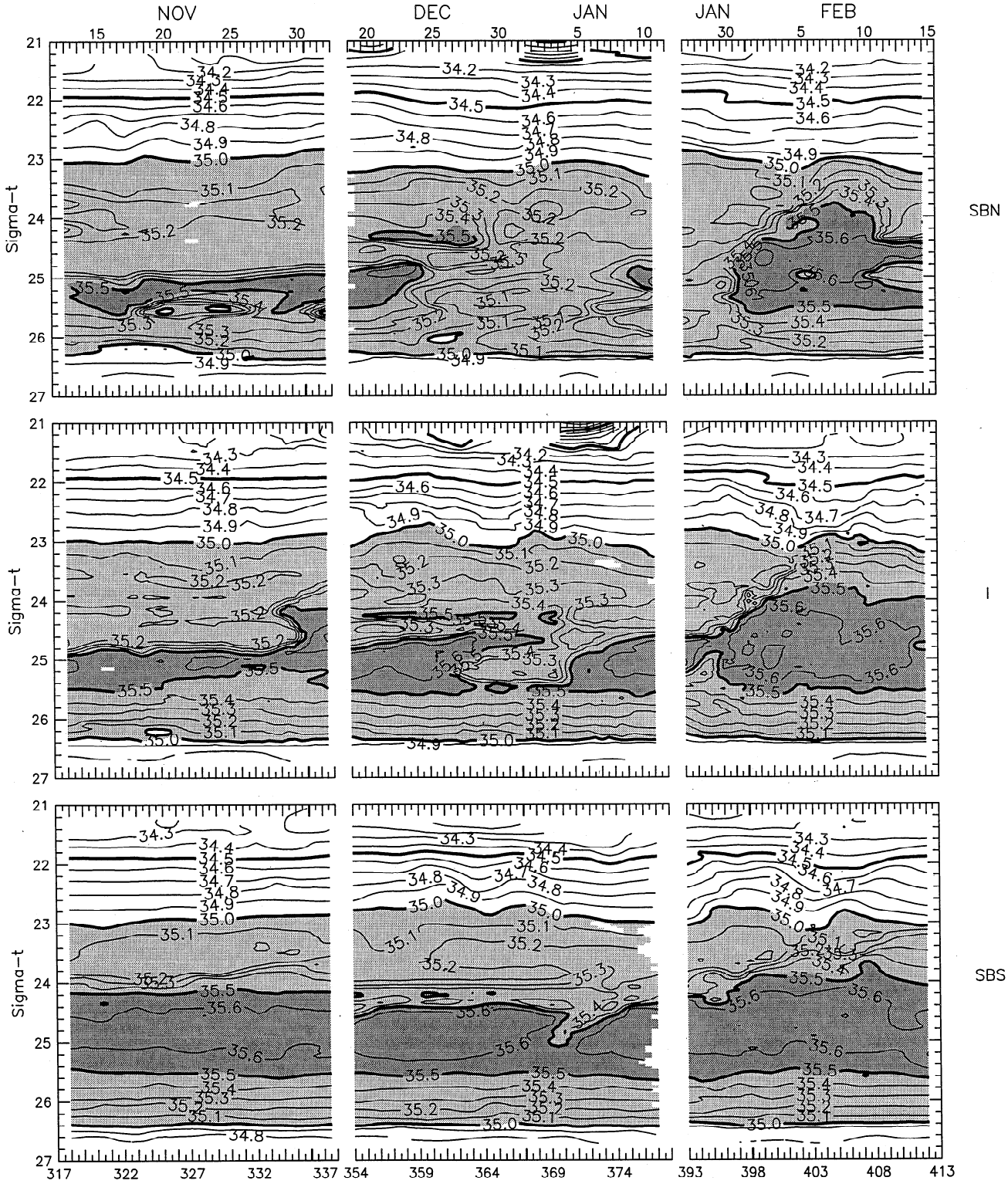

Figure 20. Variability of the salinity profile at (top) the north end (SBN), (middle) the midpoint (I), and (bottom) southern end (SBS) of the N2S line. Density rather than depth is used as the vertical axis to remove fluctuations due to internal waves.

salinity maximum (with S>35.5 psu, centered at σ_t = 25 kg m^{-3}) was nearly unchanged from November 13 to 22 and remained similar through December 2 (Figure 19). Meanwhile, a small secondary salinity inversion seen at σ_t = 24.2 kg m^{-3} and 2.25°S on November 13 developed into the intense secondary maximum at 1.5°S on December 1–2; remnants of this or a similar secondary maximum were observed along σ_t =24.2 kg m^{-3} on December 20. There is substantial eastward flow at this depth (0.2–0.3 m s^{-1} in November [*Lukas et al.*, 1995a]), and thus the observed changes may reflect zonal inhomogeneities as well as meridional variations.

Figure 20 shows that a very high salinity layer (with S_{max} usually >35.6 and always >35.5) was always present at SBS, the southern apex, where salinity almost always decreased monotonically away from the maximum, both above and below. At the midpoint (I, at 1°50′S, 156°06′E), the vertical structure was both more complex and more variable; small secondary salinity inversions emerged and faded, and the σ_t range of the layer with S >35.5 psu varied from < 0.1 to > 1 kg m^{-3} (Figure 20). Secondary salinity inversions were even more common at SBN, the northern apex, and the layer with S >35.5 psu was transient rather than persistent there. At all three locations, anomalies tend to migrate upward through the water column in the σ_t range of 25.5 to 23 kg m^{-3} (Figure 20): such upward migration is particularly obvious at SBS and I in early January

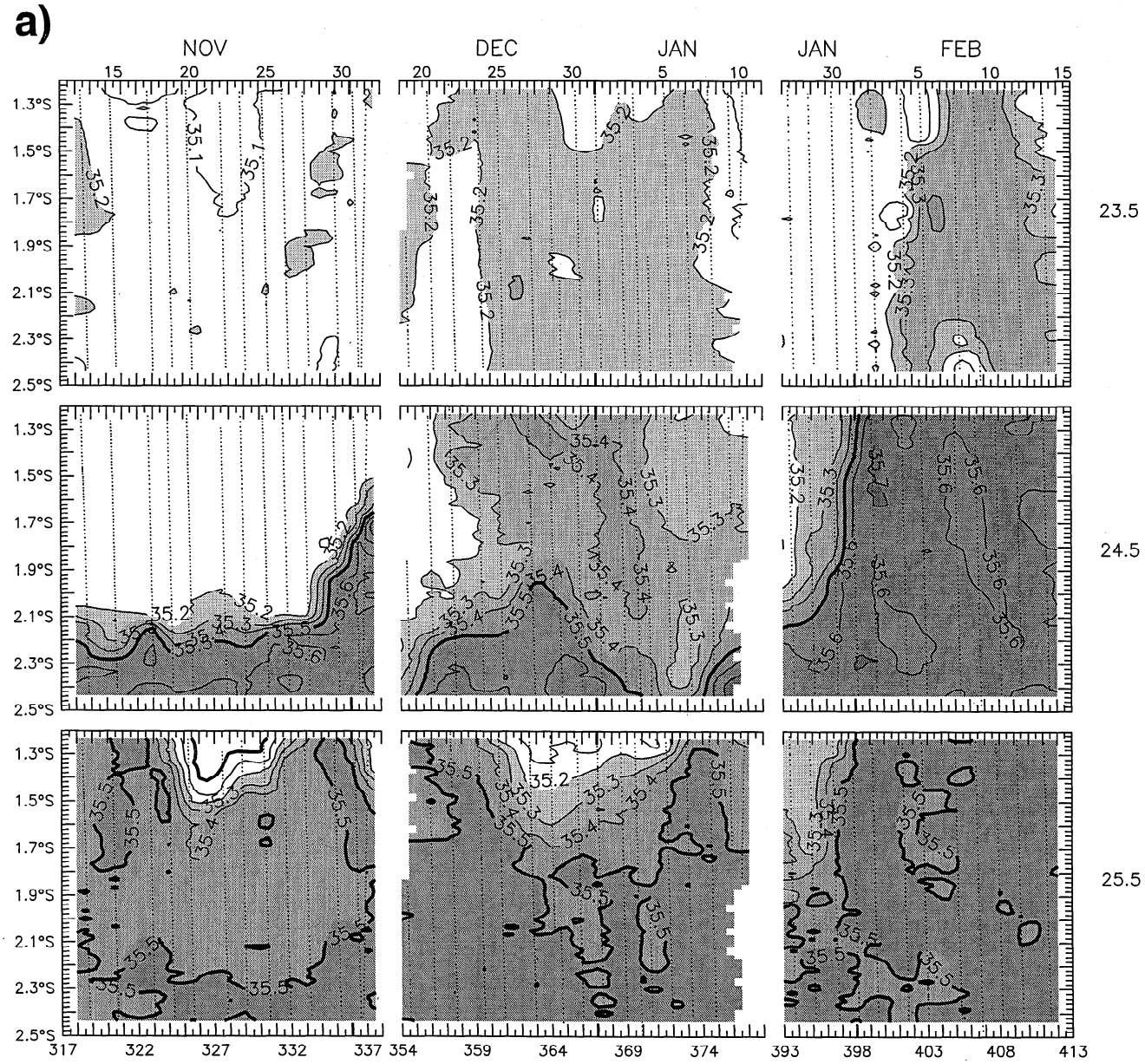

Figure 21. Variation of T-S properties on three isopycnals in the main thermocline (σ_t = 23.5, 24.5, 25.5). Contours are labeled in units of salinity; corresponding values of temperature are given in Table 5. (a) The latitude-time distributions for the N2S line along 156°06′E. (b) The longitude-time distributions for the W2E section along 1°50′S.

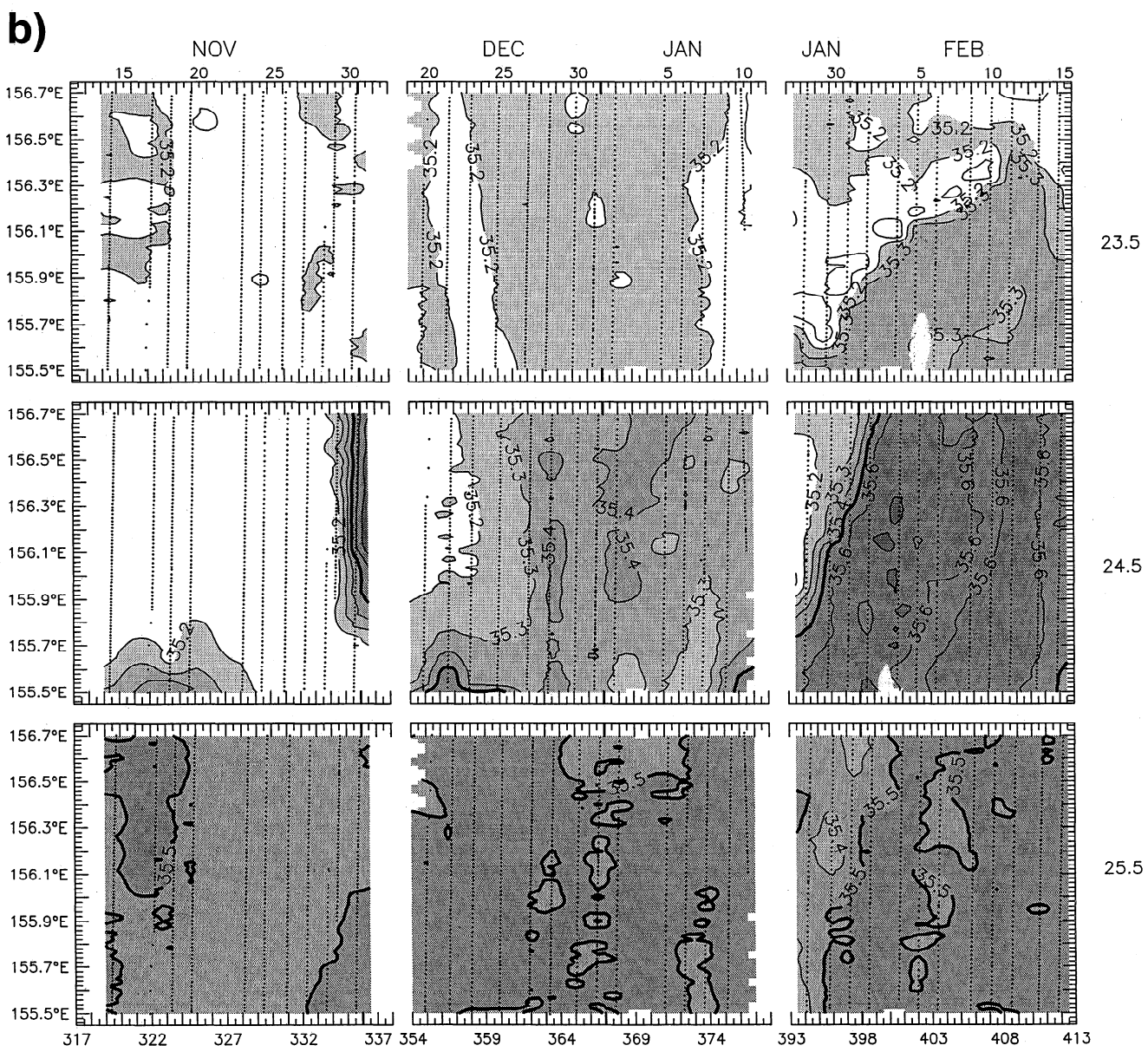

Figure 21. (continued)

(days 368–375) and at I and SBN in early February (days 395–405).

Time-latitude and time-longitude distributions of temperature-salinity characteristics on isopycnals spanning the salinity maximum are shown in Figures 21 and 22; though contours are labeled as salinity, each isohaline also represents an isotherm (Table 5). The three isopycnals shown in Figure 21 span most of the variability in T-S characteristics (Figure 18); those shown in Figure 22 lie near the core of the maximum (Figure 19).

In November, the salinity at $\sigma_t = 25.2$ was nearly uniform (Figures 18 and 22), though there were significant lateral gradients and temporal variability both above and below this high-salinity core; waters at $\sigma_t = 23.5$ were also relatively homogeneous at ~24°C, 35.15 psu (Figure 21). A thin intrusion of relatively fresh water centered at σ_t =25.5 (Figure 18) was observed along the northern portion of the N2S line from November 19 to 26, but it did not penetrate as far south as W2E line (Figures 21a and 21b). A fairly thick isohaline layer centered at about σ_t = 24.5 (Figure 18) was present throughout this period along much of the W2E line and at the northern end of the N2S line (Figure 21a and 21b). The front separating this relatively fresh isohaline intrusion from adjacent waters was narrow (10–20 km) and sharp ($\sim 2\times 10^{-5}$ psu m^{-1}); this front seemed to be stationary during November 15–19, migrating slowly eastward during November 20–24, migrating rapidly northward (at >0.1 m s^{-1}) beginning November 29, and passing the W2E line on November 30. A much more diffuse but otherwise similar front

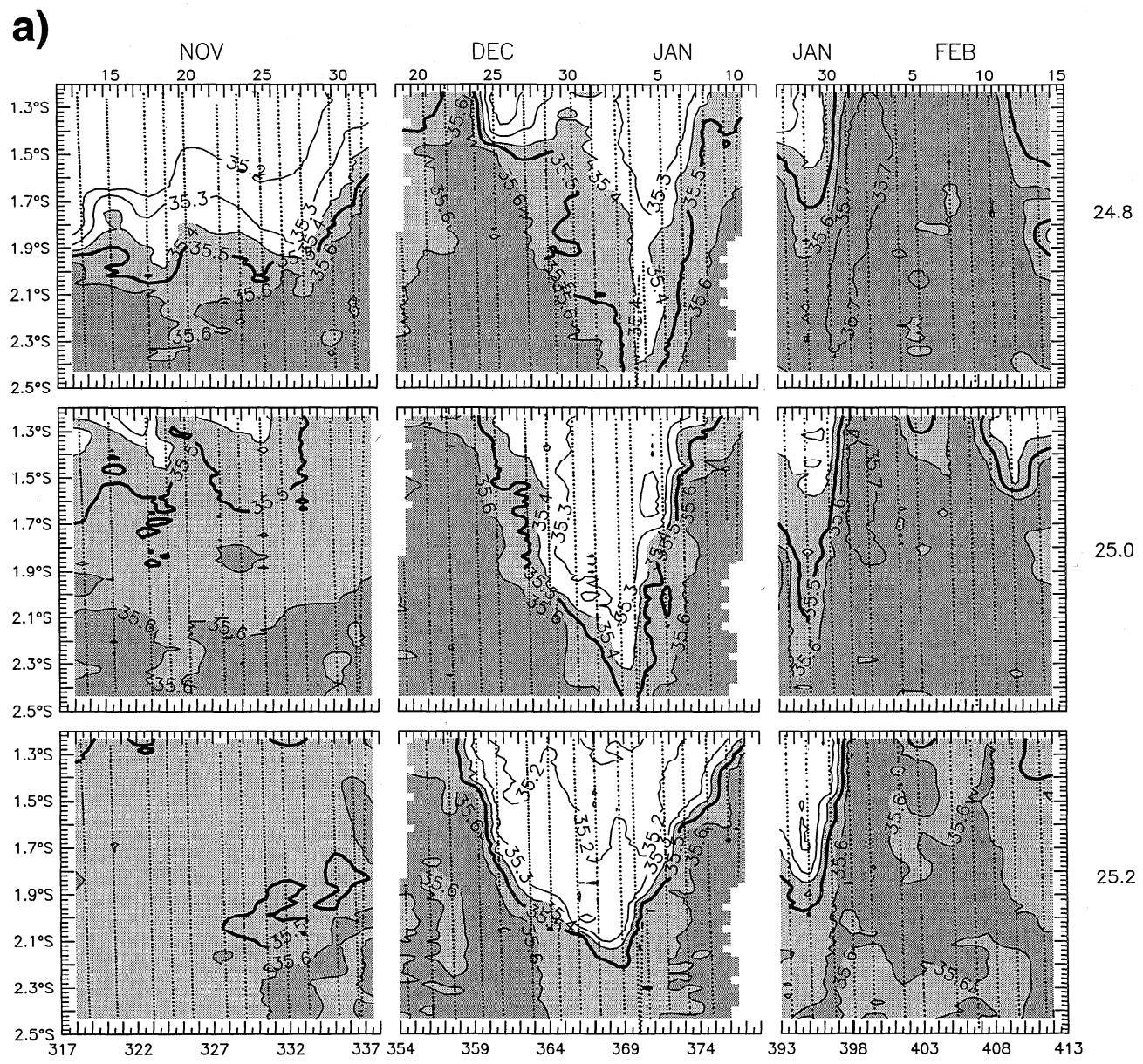

Figure 22. Variation of T-S properties on isopycnals near the core of the salinity maximum (σ_t = 24.8, 25.0, 25.2). Contours are labeled in units of salinity; corresponding values of temperature are given in Table 5. (a) The latitude-time distributions for the N2S line along 156°06′E. (b) The longitude-time distributions for the W2E section along 1°50′S.

was observed on the $\sigma_t = 24.8$ and 25.0 isopycnals (Figure 22) at the lower limit of this intrusion (Figure 18). Northward migration of the front coincided with net northward currents in the layer between 110 and 180 m [*Lukas et al.*, 1995a].

In late December and early January, water properties on $\sigma_t = 23.5$ were again nearly uniform, though the salinity was slightly higher (by 0.1 psu) than in November (Figure 21). Relatively fresh water again intruded from the north (in late December) into waters of uniformly high salinity (35.5–35.6 psu) between the σ_t = 24.8 and $\sigma_t = 25.5$ isopycnals, and withdrew again in early January (Figures 19, 21, and 22); the freshest water was centered at $\sigma_t = 25.2$. The front was narrowest and most intense at this density; above and below the core of the intrusion, the front intersected isopycnals at an oblique angle (Figure 19). This front migrated southward in late December and northward in early January (Figure 22a). Typical meridional migration rates were about 10 km d^{-1} (0.1 m s^{-1}), consistent with typical meridional ADCP currents at this depth [*Lukas et al.*, 1995a]. The front also migrated generally eastward (Figure 22b), with typical speeds of 20–30 km d^{-1} (0.2–0.3 m s^{-1}); these are consistent with the average eastward velocities measured at the depth of the salinity maximum (Figures 7 and 10).

During much of the third survey period, maximum salinities were >35.5 psu over large portions of both the

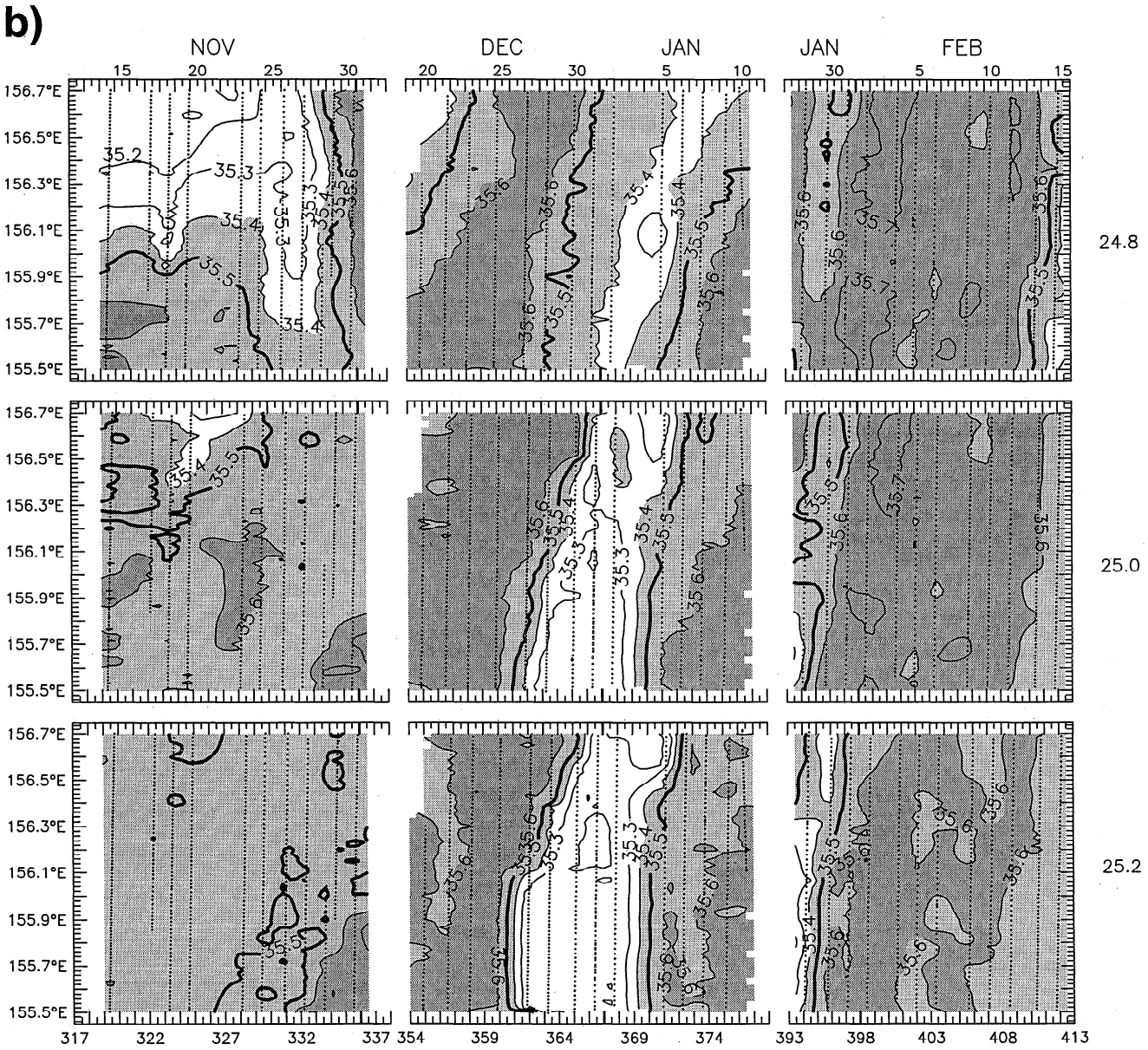

Figure 22. (continued)

N2S and W2E sections (Figures 19, 21, and 22) and over a large range of densities (σ_t = 24.5 to 25.2). Intrusions of relatively fresh water from the north occurred at the beginning and end of this period (in late January and mid-February), and the frontal structure and migration rates were similar to those observed earlier.

The migration of these relatively large watermass features (extending >20 km laterally and >20 m vertically, or >0.2 kg m^{-3} in density) seems to be governed by the ambient currents. Smaller, very subtle features can also be coherent in both space and time. For example, the "waterfall" plot of salinity profiles in Figure 23 shows that a very small (<0.04 psu) salinity inversion at σ_t = 21.8 extending for >130 km on February 4 (from 1.25°to 2.4°S) is still present 32 hours later. Other similarly subtle features are spatially coherent over as few as three or four adjacent Seasoar profiles (i.e., <12 km), as seen at σ_t = 24.6 just left of the center of the February 4 section. Most of these subtle features extend for >40 km, and most lie on a line or curve that lies oblique to the isopycnals. Features are observed both above and below the maximum salinity, i.e., in the regime that is diffusively stable as well as in the regime that is favorable for salt fingering. The generation, evolution, and decay of these small features are very likely affected by the complex equatorial flow field, in which internal tides and other baroclinic waves are superimposed on the highly sheared mean currents, but further study of these processes is beyond the scope of this paper.

6. Discussion

6.1. The Surface Layer

Since all atmosphere-ocean interactions are inevitably mediated through the surface of the ocean, the ocean surface layer is the focus of special attention within

Table 5. Values of Temperature Corresponding to Specific Values of Salinity on the Isopycnal Surfaces with σ_t = 23.5, 24.5, 24.8, 25.0, 25.2, and 25.5 kg m^{-3}

	Temperature at Isopycnal, °C					
S, psu	$\sigma_t = 23.5$	$\sigma_t = 24.5$	$\sigma_t = 24.8$	$\sigma_t = 25.0$	$\sigma_t = 25.2$	$\sigma_t = 25.5$
35.2	24.98	21.54	20.44	19.68	18.91	17.70
35.3	25.23	21.82	20.72	19.97	19.20	18.02
35.4	25.48	22.09	21.00	20.26	19.50	18.32
35.5	25.72	22.36	21.28	20.54	19.79	18.63
35.6	25.96	22.62	21.56	20.83	20.08	18.93

COARE [*Webster and Lukas,* 1992; *Tomczak,* 1995; *You,* 1995; *Anderson et al.,* 1996]. Definitions of this surface layer abound [*Brainerd and Gregg,* 1995; *Lukas and Lindstrom,* 1991], and its depth is affected by a variety of processes: diurnal heating due to solar radiation; cooling at the surface by evaporation, sensible heat flux, and long wave radiation; nocturnal convection due to surface cooling; stirring by the local wind stress or by shear instabilities; restratification by the addition of cool but fresh water from rainfall; and differential advection from/to the surrounding ocean. Near-surface fields of temperature and salinity have been presented and discussed earlier in this paper, in the form of cruise-averaged and individual meridional sections (Figure 9,

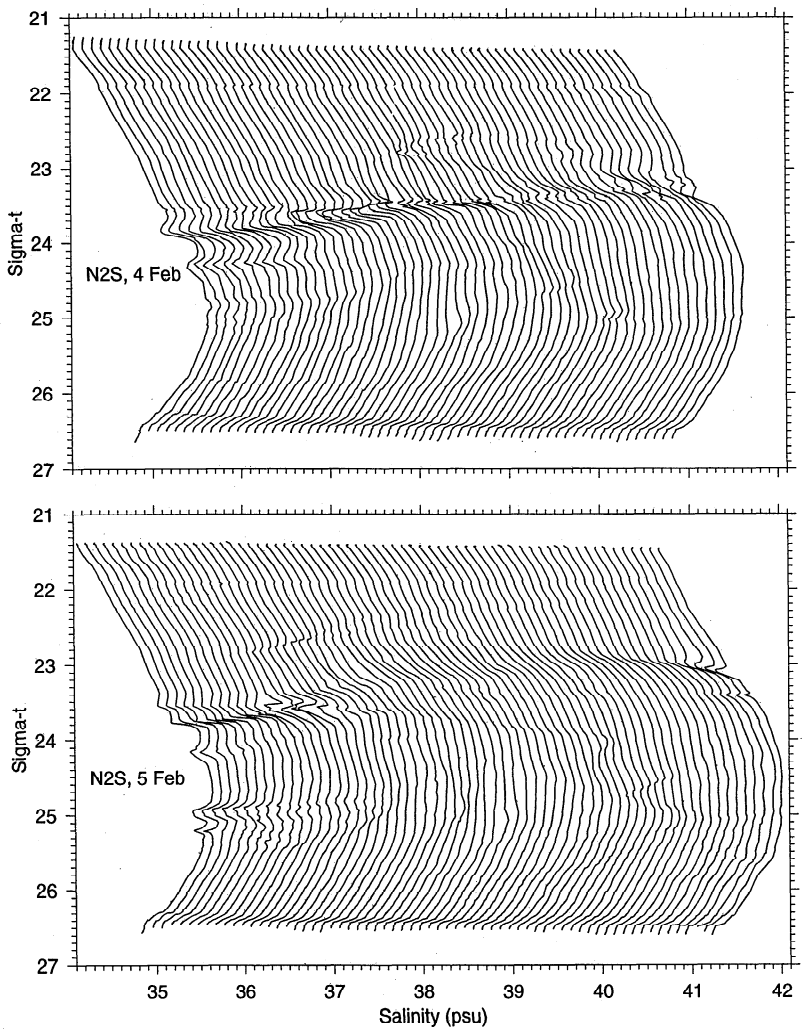

Figure 23. Salinity profiles showing 1-Hz data from adjacent ascending Seasoar profiles from consecutive sections along 156°06′E. Sections were run from 1°14′S (on the right) to 2°26′S (on the left), beginning (top) at 0604 UT on February 4 and (bottom) at 1425 UT on February 5. Axis labels apply to the northernmost profile; successive profiles are offset by 0.1 psu for display and are usually separated by <2.5 km.

Plates 1 and 2), time-depth distributions for the intersection (Figure 12), time-distance distributions for the 20-dbar surface (Figures13a and 13b), and time series of laterally averaged statistics (Figure 14), but we have not yet discussed the structure of the mixed layer per se. Here we explicitly consider the vertical structure of the near-surface layer, by estimating the surface layer depths using several different criteria.

Surface "mixed" layer depth can be defined in terms of a finite change from values at the surface [e.g., *Anderson et al.*, 1996; *Wijesekera and Gregg*, 1996; *Smyth et al.*, 1996b], in terms of a critical gradient [e.g., *Lukas and Lindstrom*, 1991], or even in terms of a specific isopycnal [e.g., *Smyth et al.*, 1996b]. We estimate "mixed layer" depths from the 2-dbar, 2-nm gridded Seasoar data using all three of these general classes. The first of these, H_{22}, defined by the depth of the σ_θ = 22.0 kg m^{-3} isopycnal, corresponds to the "upper ocean layer" used by *Smyth et al.* [1996b] to represent the region above the main pycnocline; this isopycnal is nearly coincident with the 28°C isotherm (Figure 15). The second, H_t, estimates the depth of the "top of the thermocline" from a critical gradient criterion of 0.05°C m^{-1} but ignoring the top 20 m [*Lukas and Lindstrom*, 1991]. For the remaining layers, defined in terms of differences from the surface, we used the shallowest gridded value above 10 m to represent the surface value; it was usually centered at 0.5 or 2 m. The "isopycnal layer depth," H_D, is defined as the depth at which the potential density first exceeds the surface density by $\Delta\sigma_\theta = 0.01$ kg m^{-3}. This layer is sometimes called the "diurnal mixed layer" [*Smyth et al.*, 1996b]. The "isothermal layer depth", H_T, and "isohaline layer depth", H_S, are defined separately, by $\Delta T = -0.030°$ C $= \alpha^{-1}\Delta\sigma_\theta$ and $\Delta S = 0.013$ psu $= -\beta^{-1}\Delta\sigma_\theta$, respectively, where α and β are the thermal and haline expansion coefficients at 28°C and 35 psu. Following *Anderson et al.* [1996], we calculated H_T (and H_S) by finding the maximum temperature (minimum salinity) in the top 20 m and starting the differencing from that

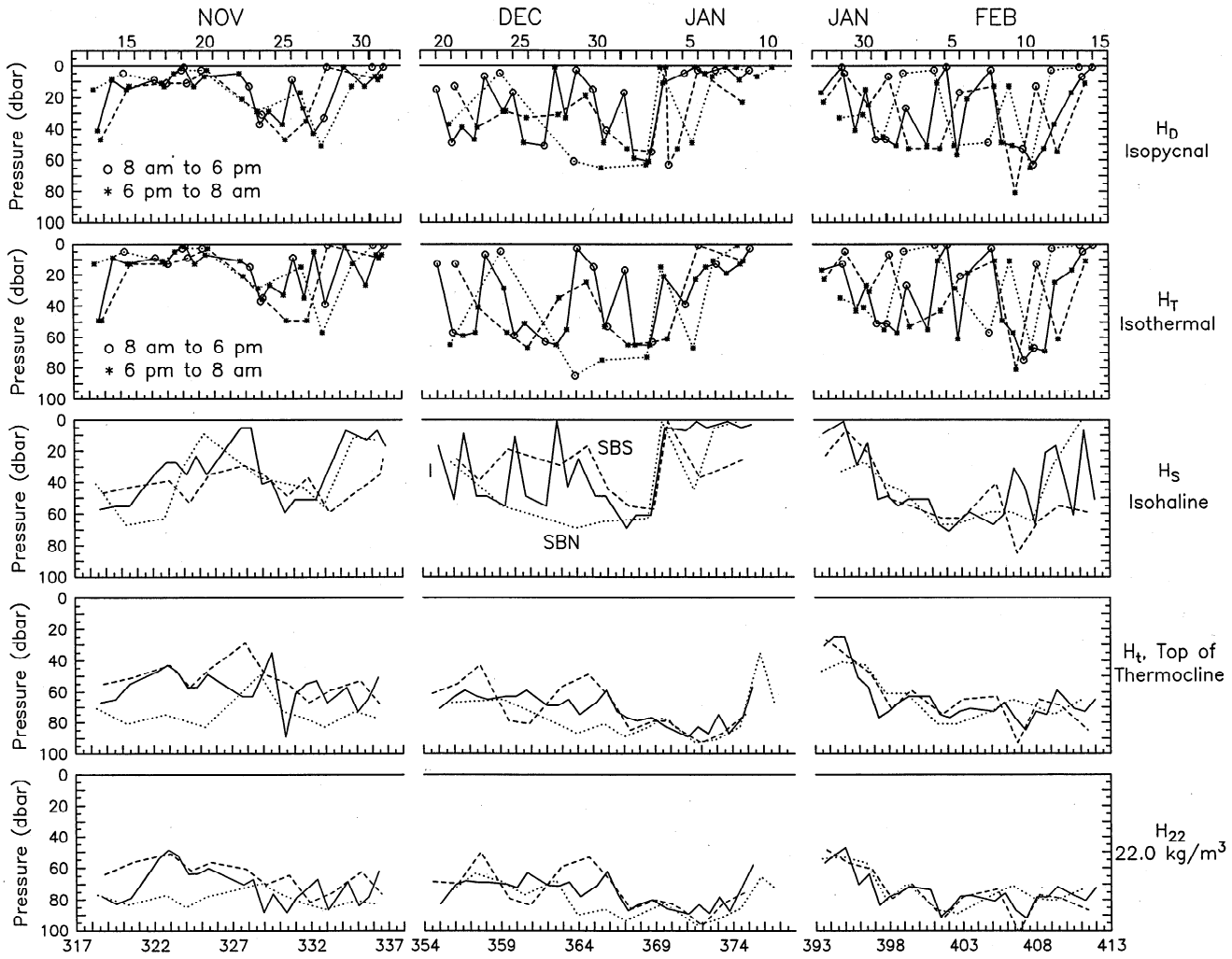

Figure 24. Time series of surface layer depths at three locations (SBN (dotted lines), SBS (dashed lines) and I (solid lines)), estimated from 2-dbar gridded Seasoar data using criteria specified in the text. Symbols are used to distinguish daytime and nighttime estimates of H_D and H_T.

point downward to prevent near-surface inversions from influencing our estimates.

Estimates of these surface layer depths were made for all of the complete meridional and zonal Seasoar sections. Figure 24 shows time series of the values at the intersection point (I) and at the northern and southern apices (SBN and SBS). In general, each layer shows similar behavior at all three locations. H_D and H_T are subject to strong diurnal variability as expected [*Anderson et al.*, 1996], except during periods of weak winds combined with either sustained heating (November 15 to 22, November 29 to December 1) or heavy precipitation (Jan 4–10). There is a tendency for smaller values of H_D and H_T to occur during daytime and deeper values to occur at night, but exceptions are not uncommon (Figure 24). H_S tends to shoal during the November survey period and to deepen during the westerly wind burst in late December, before shoaling abruptly in response to heavy rainfall in early January; it deepens rapidly in unison with H_t and H_{22} (Figure 24) during January 27–31, apparently downwelling in response to the renewed westerly wind stress (Figure 14). There is a tendency for H_t and H_{22} (and the 28°C isotherm, Figure 16) to be deeper in the north, particularly during our November survey period and during the westerly wind burst in late December.

At all three locations, the top of the thermocline, H_t, lies above the 22.0 kg m^{-3} isopycnal (Figures 24 and Figure 25). Their separation is <10 m during much of our second survey period, during and after the strong westerly wind burst. The two converge completely on January 4–6, after the cessation of the strong westerly winds and while the overlying water is restratified by rainfall (Figures 24 and 25). The top of the thermocline is always deeper than the surface "isohaline" layer, H_S (Figure 24), but the "barrier layer" [*Lukas and Lindstrom*, 1991] that lies between them is sometimes <10 m thick. By definition, the isopycnal layer, H_D, is equal to or less than H_S and H_T. The "isothermal" layer, H_T, is often deeper than H_S, presumably because subsequent precipitation has overlain a remnant mixed layer; it should be noted that these layers need not be strictly homogenous. The frequent occurrences of $H_T > H_S$ suggest that at least the upper portion of the barrier layer is transient or patchy in nature. Nevertheless, H_T approaches within 10 m of H_t on only a few brief occasions (December 20–22, December 25–28, December 31, February 10–11) of strong westerly winds, and H_T and H_t do not coincide on any occasion. Thus the lower portion of the barrier layer effectively insulated the sea surface from direct exchange with the cooler waters in the thermocline throughout the COARE IOP.

6.2. Lateral Homogenization

In section 5.1. we noted that property distribution on the 20-dbar surface (Figure 13) suggested an association between the degree of patchiness and the strength of the wind: standard deviations along each section were relatively large during the weak winds of November and early January and small during the westerly wind burst in December and the squalls in early Febru-

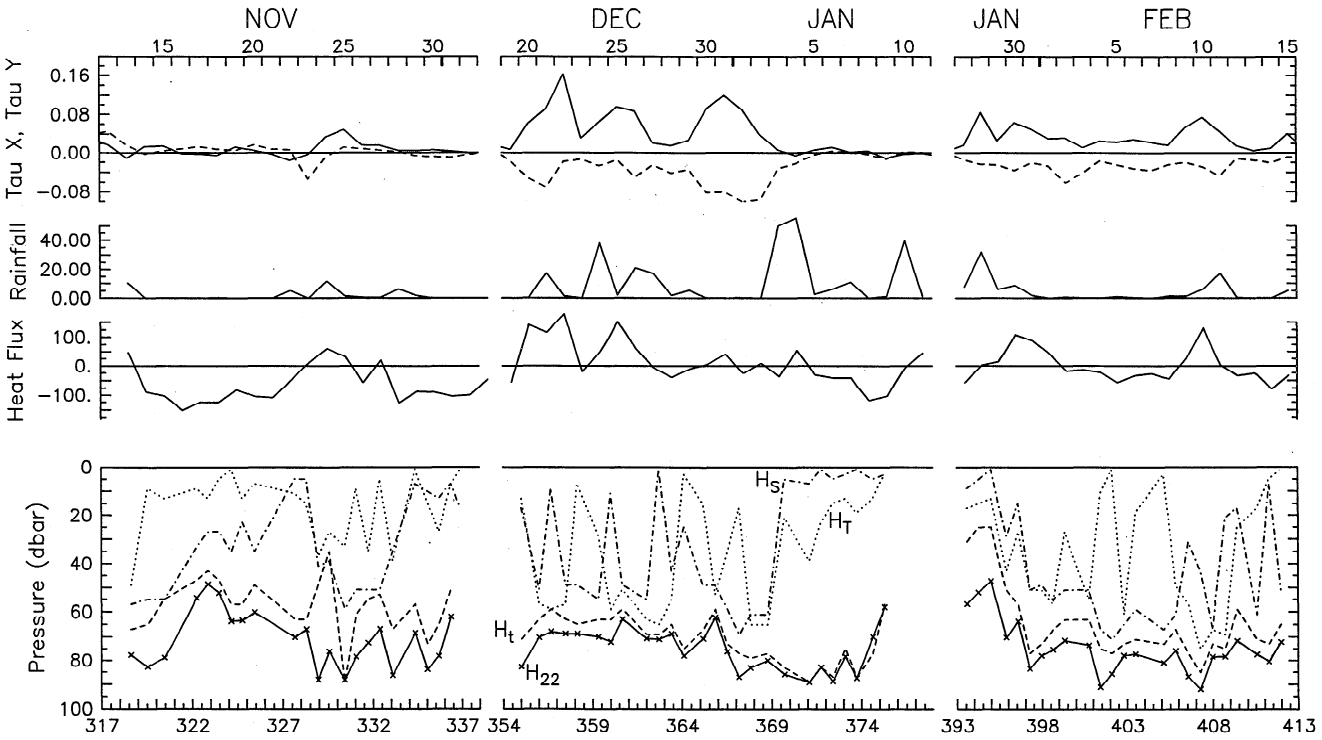

Figure 25. Variation of surface layer depths at the intersection I (1°50′S, 156°06′E), estimated from 2-dbar gridded Seasoar data; time series of wind stress, rainfall, and heat flux are repeated from Figure 12.

ary (Figure 14). Although this isobar does not always lie within the surface mixed layer as defined by either H_D or H_T (Figures 24 and 25), it is usually shallower than the daily maximum [*Anderson et al.*, 1996, Figure 6], and thus it represents, at least approximately, the nocturnal surface mixed layer. The apparent relation between the degree of patchiness and the strength of the wind (Figure 14) is verified by scatter diagrams (Figure 26), which show larger spatial variance to be associated with weak zonal wind stress; similar results are obtained for the meridional wind stress and for the wind stress magnitude, since winds were predominantly from the northwest throughout the IOP. Strong winds seem to reduce meridional trends as well as the residual patchiness in both zonal and meridional directions (Figure 26). Whether this homogenization results from large-scale accumulation of surface water and broad equatorial downwelling driven by the westerly winds or whether it is the result of lateral mixing by small-scale processes such as local convergences driven by squalls is not clear.

6.3. The Thermocline, EUC, and Salinity Maximum

The structure and properties of the main thermocline were surprisingly variable, on timescales ranging from days to weeks and months. Some of the variability in the upper thermocline was related to variations in the

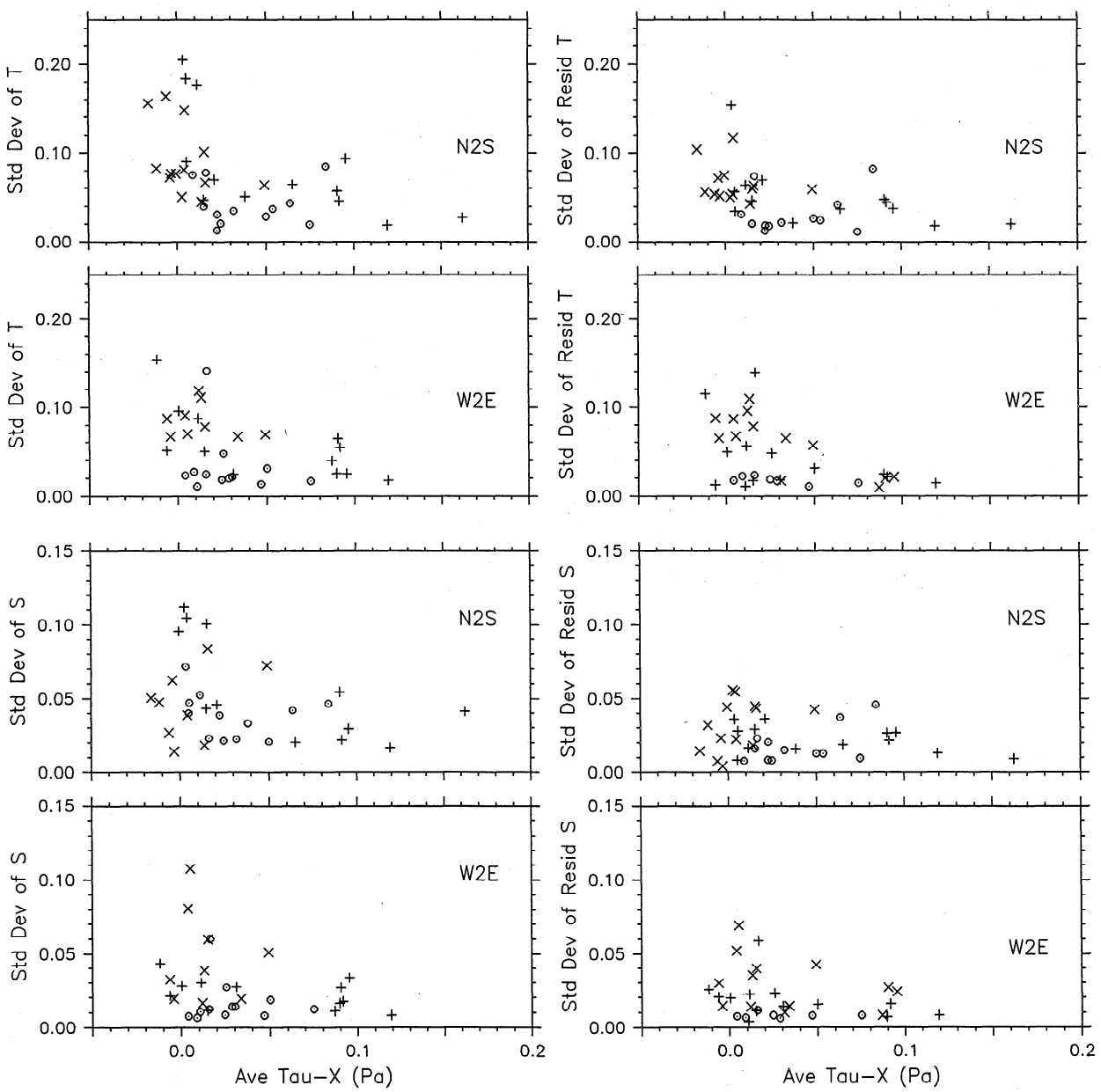

Figure 26. Lateral standard deviations of 20-dbar temperature and salinity versus the average zonal wind stress for the preceding 24-hour period; results are shown for both observed values and values detrended by linear regression versus latitude or longitude. Different symbols distinguish data from the three survey periods: W9211A (crosses), W9211B (pluses) and W9211C (circles).

zonal wind stress, but we also observed variations that were not related to local winds; this is hardly surprising, since long equatorial waves are known to be efficient conveyors of signals from the central Pacific [e.g., *Kessler and McPhaden,* 1995]. Some of the variations, e.g., the degree of equatorward spreading between the upper and lower thermocline, are related to the strength and position of the Equatorial Undercurrent, and the undercurrent is clearly important in advecting waters eastward in and along the core of the salinity maximum: we do not yet fully understand the dynamics which determine the depth and the temperature of the core of the undercurrent, nor do we know what governs the properties of its source waters.

7. Summary and Conclusions

The COARE survey cruises have provided a large set of repeated 130-km meridional and zonal sections at the center of the COARE intensive flux array. These sections have fine vertical (~2 dbar) and horizontal (~2 nm) resolution and extend to a depth of ~280 dbar. Observations were repeated at intervals of ~2 days during three 20-day periods, spanning most of the 4-month COARE intensive observation period from November 1992 to February 1993.

Our time-averaged fields show a number of features that are typical of the western equatorial Pacific Ocean: a very warm and relatively fresh surface layer, with temperatures >28.5°C and salinity decreasing northward; a very sharp thermocline with temperature decreasing from ~28°C at ~50 m to ~12°C at ~250 m and intermediate isotherms diverging northward toward the equator to envelop the core of the Equatorial Undercurrent at ~175 m; a subsurface salinity maximum, consisting of a northward tending tongue of high-salinity South Pacific water; and a deep vertically mixed layer, ~50 m thick, with a temperature of ~12°C and salinity of 34.8 psu, corresponding to the equatorial thermostad.

The duration of the COARE Intensive Observation Period was exceptionally long for an intensive study of the upper ocean, but this was clearly appropriate given the lack of stationarity in both atmospheric and oceanic regimes. In general, near-surface temperature responded as expected from the variations in the local winds: general heating during the calm winds in November, rapid cooling during the westerly wind burst in late December, warming during weak easterly winds in January, and gradual cooling during moderate westerlies in February. Variations in the depth of the 28°C isotherm and the 22.0 kg m^{-3} isopycnal at the top of the thermocline also varied with the wind: deepening during the westerly wind burst, shoaling during the easterlies in January, and deepening rapidly with the resumption of westerly winds in early February. Vertical stratification within the near-surface layer varied with wind stress and rainfall: thermal stratification was strong under calm winds in November, and salinity stratification was strong under calm winds and heavy rainfall in early January; both thermal and haline stratification were weak during the westerly wind burst in late December and the moderate winds in February. Unexpectedly, we also observed some mesoscale features with strong lateral gradients in the near-surface layer: most notably, a zonal temperature front (with ΔT of ~0.2°C in ~10 km) that migrated northward during the westerly wind burst in late December and a small patch or narrow band (~40 km wide) of unusually cold water (<28.5°C) that migrated slowly northward during January 5–9, the nature and origin of these features is still not fully understood. Also unexpected was the observation that strong winds seemed to cause lateral homogenization of near-surface waters as well as vertical mixing.

Within the main thermocline, isotherm depths varied from section to section and from cruise to cruise. High-frequency internal waves and tides, though not resolved by our sampling pattern, were manifest as noise with vertical displacements of ~10 m. Cruise-averaged sections show that both the equatorward spreading of isotherms and the Equatorial Undercurrent shoaled significantly during the 100-day observation period; while the core layer shoaled from ~220 to ~160 m, its temperature increased from ~14°to ~20°C. The separation between the 23°C and 14°C isotherms in the upper and lower thermocline spreading seemed to be greatest (>120 m) during periods when the EUC was strong (>0.4 m s^{-1}). Water mass characteristics of the salinity maximum within the thermocline were surprisingly variable: maximum salinity values ranged from ~35.2 to ~35.7 psu. The front between high-salinity southern and low-salinity northern waters was often narrow (~30 km), and it migrated meridionally between and within cruises; this front was also observed to migrate eastward at a speed consistent with advection by the Equatorial Undercurrent. Secondary salinity inversions with lateral scales of 10–50 km were observed both above and below the high-salinity core; these were easily recognizable in sections a few days apart but did not persist from cruise to cruise.

This large, high-resolution Seasoar data set shows that the thermohaline fields in the COARE intensive flux array are both heterogeneous and nonstationary. Even within the broadly uniform Warm Pool of the western equatorial Pacific, there are instances of mesoscale and submesoscale fronts in the surface layer. We look forward to combining this data set with observations from other survey ships and with time series from stationary platforms. Work to estimate advective heat and freshwater fluxes and three-dimensional budgets of heat, fresh water, and momentum and to study the evolution of particular features and phenomena is underway. This large data set will provide many opportunities to improve community understanding of the upper ocean dynamics in this region.

Acknowledgments. We are deeply indebted to COARE Surveys co-investigators Clayton Paulson and Eric Firing, who participated fully in the cruise planning and data collection. We are also indebted to *Wecoma*'s Marine Technicians (Marc Willis, Brian Wendler, Mike Hill, and Tim Holt) for the successful operation of the Seasoar system and to Robert O'Malley and Jane Fleischbein for archiving and processing the data and assistance in analysis. We are also grateful to every cruise participant and to the officers and crew of *Wecoma*. Processed ADCP data were provided by Eric Firing. Meteorological data were provided by Robert Weller and Melora Park (WHOI) and by Clayton Paulson and Lynne deWitt (OSU). We are grateful for frequent discussions with Eric Antonissen, Bill Smyth, Clayton Paulson, and Hemantha Wijesekera. This work was supported by the Ocean Sciences Division of the National Science Foundation and by the NOAA Office under TOGA through NSF grants OCE-9113510 and OCE-9113948.

References

Anderson, S. P., R. A. Weller, and R. B. Lukas, Surface buoyancy forcing and the mixed layer of the western Pacific Warm Pool: Observations and 1-D model results, *J. Clim., 9*, 3056–3085, 1996.

Brainerd, K. E., and M. C. Gregg, Surface mixed and mixing layer depths, *Deep Sea Res., Part I, 42*, 1521–1543, 1995.

Eldin, G, T. Delcroix, C. Henin, K. Richards, Y. Du Penhoat, J. Picaut, and P. Rual, Large-scale current and thermohaline structures along 156°E during the COARE intensive observation period, *Geophys. Res. Lett., 21*, 2681–2684, 1994.

Eriksen, C. C., A. J. Plueddemann, and R. A. Weller, Advection and local change of temperature and salinity in the COARE Intensive Flux Array estimated from a 3-mooring array, in *Summary Report of the TOGA COARE International Data Workshop*, Toulouse, France, 2–11 August 1994, pp. 100, TOGA COARE International Project Office, Univ. Corp. for Atmos. Res., Boulder, Colo., 1995a.

Eriksen, C. C., A. J. Plueddemann, and R. A. Weller, Tidal prediction of current and vertical displacement in the COARE IFA estimated from a 3-mooring array, in *Summary Report of the TOGA COARE International Data Workshop*, Toulouse, France, 2–11 August 1994, pp. 101, TOGA COARE International Project Office, Univ. Corp. for Atmos. Res., Boulder, Colo., 1995b.

Gill, A. E., *Atmosphere-Ocean Dynamics*, Academic, San Diego, Calif., 1982.

Halpert, M. S., G. D. Bell, V. E. Kousky, and C. F. Ropelewski (Eds.), *Fifth Annual Climate Assessment 1993*, 111 pp., Natl. Oceanic and Atmos. Admin., U. S. Dep. of Commer., Clim. Anal. Cent., Washington, D. C., 1994.

Huyer, A., P. M. Kosro, R. O'Malley, and J. Fleischbein, SEASOAR and CTD observations during a COARE Surveys cruise, W9211C, 22 January to 22 February 1993, *Data Rep. 154, Ref. 93-2*, 325 pp., Coll. of Oceanic and Atmos. Sci., Oreg. State Univ., Corvallis, 1993.

Huyer, A., P. Hacker, P. M. Kosro, J. Fleischbein, E. Antonissen, and R. O'Malley, SEASOAR and CTD observations during a COARE Surveys cruise, W9211A, 8 November to 8 December 1992, *Data Report 155, Ref. 94-1*, 364 pp., Coll.of Oceanic and Atmos. Sci., Oreg. State Univ., Corvallis, 1994.

Kaneko, A., N. Gohda, H. Nakajima, T. Itoh, K. Kawatate, T. Nagahama, and H. Furukawa, Profiling measurement of the equatorial currents by an ADCP on the mooring lines, in *Preliminary report of the Hakuho Maru Cruise KH-92-5 (TOGA/COARE Cruise)*, edited by T. Asai, pp. 36–55, Ocean Research Institute, University of Tokyo, Tokyo, 1993.

Kessler, W. S., and M. J. McPhaden, Oceanic equatorial waves and the 1991-3 El Niño, *J. Clim., 8*, 1757–1774, 1995.

Kutsuwada, K., and H. Inaba, Year-long measurements of upper-ocean currents in the western equatorial Pacific by acoustic Doppler current profilers, *J. Meteorol. Soc. Jpn, 73*, 399–409, 1995.

Lueck, R., Thermal inertia of conductivity cells: Theory, *J. Atmos. Oceanic Techol., 7*, 741–755, 1990.

Lueck, R., and J. J. Picklo, Thermal inertia of conductivity cells: Observations with a Sea-Bird cell, *J. Atmos. Oceanic Technol., 7*, 756–768, 1990.

Lukas, R., and P. Hacker, Spinup of a submesoscale eddy in the TOGA COARE intensive flux array during the spindown of an eastward jet, paper presented at the TOGA 95, International Science Conference, World Meteorol. Organ., Melbourne, Australia, April 1995.

Lukas, R., and E. Lindstrom, The mixed layer of the western equatorial Pacific Ocean, *J. Geophys. Res., 96*, suppl., 3343–3357, 1991.

Lukas, R., P. Hacker, M. Mao, E. Firing, A. Huyer, and P.M. Kosro, Upper ocean currents in the intensive flux array during TOGA COARE, in *Proceedings of TOGA 95 Int'l Sci. Conf., April 1995, WRCP-91-WMO/TD 717*, vol.1, pp. 542–546, World Meteorol. Organ., Geneva, Switzerland, 1995a.

Lukas, R., P. J. Webster, M. Ji, and A. Leetmaa, The large-scale context for the TOGA Coupled Ocean-Atmosphere Response Experiment, *Meteorol. Atmos. Phys., 56*, 3–16, 1995b.

McPhaden, M. J., TOGA-TAO and the 1991-93 El Niño-Southern Oscillation event, *Oceanography, 6*, 36–44, 1993.

McPhaden, M. J., Ocean-atmosphere variability observed from the TOGA-TAO array, in *Proceedings of TOGA 95 Int'l Sci. Conf., April 1995, WRCP-91 - WMO/TD 717*, vol. 1, pp. 181–185, World Meteorol. Organ, Geneva, Switzerland, 1995.

McPhaden, M. J., S. P. Hayes, L. J. Mangum, and J. M. Toole, Variability in the western equatorial Pacific Ocean during the 1986-87 El Niño-Southern Oscillation event, *J. Phys. Oceanogr., 20*, 172–190, 1990.

McPhaden, M. J., F. Bahr, Y. du Penhoat, E. Firing, S. P. Hayes, P. P. Niiler, P. L. Richardson, and J. M. Toole, The response of the western equatorial Pacific Ocean to westerly wind bursts during November 1989 to January 1990, *J. Geophys. Res., 97*, 14,289–14,303, 1992.

Morison, J., R. Andersen, N. Larson, E. D'Asaro, and T. Boyd, The correction for thermal lag effects in Sea-Bird CTD data, *J. Atmos. Oceanic Technol., 11*, 1151–1164, 1994.

Moum, J. N., and D. R. Caldwell, Experiment explores the dynamics of ocean mixing, *Eos Trans. AGU, 75(42)*, 489, 490, 495, 1994.

O'Malley, R., P. M. Kosro, R. Lukas, and A. Huyer, Seasoar observations during a COARE Surveys cruise, W9211B, 12 December 1992 to 16 January 1993, *Data Rep. 156, Ref. 94-2*, 426 pp., Coll. of Oceanic and Atmos. Sci., Oreg. State Univ., 1994.

Parsons, D., et al., The integrated sounding system: Descriptions and preliminary observations from TOGA-COARE, *Bull. Am. Meteorol. Soc., 75*, 553–567, 1994.

Plueddemann, A. J., and R. A. Weller, Observations of the upper-ocean velocity structure from the central mooring of the TOGA COARE IFA (abstract), *Eos Trans. AGU, 75*(3), Ocean Sci. Meet. Suppl., 185, 1994.

Pollard, R., Frontal surveys with a towed profiling con-

ductivity/temperature/depth measurement package (SeaSoar), *Nature, 232*, 433–435, 1986.

Richards, K. J., and R. T. Pollard, Structure of the upper ocean in the western equatorial Pacific, *Nature, 350*, 48-50, 1991.

Sea-Bird Electronics, Inc., Bellevue, Wash., *CTD Data Acquisition Software, SEASOFT Version* 4.015, 1992.

Smyth, W. D., D. Hebert, and J. N. Moum, Local ocean response to a multiphase westerly windburst, 1, Dynamic response, *J. Geophys. Res., 101*, 22,495–22,512, 1996a.

Smyth, W. D., D. Hebert, and J. N. Moum, Local ocean response to a multiphase westerly windburst, 2, Thermal and freshwater responses, *J. Geophys. Res., 101*, 22,513–22,533, 1996b.

Tomczak, M., Salinity variability in the surface layer of the tropical western Pacific Ocean, *J. Geophys. Res., 100*, 20,499–20,512, 1995.

Toole, J. M., E. Zou, and R. C. Millard, On the circulation of upper waters in the western equatorial Pacific Ocean, *Deep Sea Res., Part A, 35*, 1451–1482, 1988.

Tsuchiya, M., The origin of the Pacific equatorial 13°C water, *J. Phys. Oceanogr., 11*, 794–812, 1981.

Tsuchiya, M., R. Lukas, R. A. Fine, E. Firing, and E. Lindstrom, Source waters of the Pacific Equatorial Undercurrent, *Progr. Oceanogr., 23*, 101–147, 1989.

Webster, P. J., and R. Lukas, TOGA COARE: The Coupled Ocean-Atmosphere Response Experiment, *Bull. Amer. Meteorol. Soc., 73*, 1378–1416, 1992.

Weller, R. A., and S. P. Anderson, Surface meteorology and air-sea fluxes in the western equatorial Pacific warm pool during the TOGA Coupled Ocean-Atmosphere Response Experiment, *J. Clim., 9*, 1959–1990, 1996.

Wijesekera, H. W., and M. G. Gregg, Surface layer response to weak winds, westerly bursts, and rain squalls in the western Pacific Warm Pool, *J. Geophys. Res., 101*, 977–997, 1996.

You, Y., Salinity variability and its role in the barrier layer formation during TOGA-COARE, *J. Phys. Oceanogr., 25*, 2778–2807, 1995.

A. Huyer and P. M. Kosro, College of Oceanic and Atmospheric Sciences, Oregon State University, 104 Ocean Administration Building, Corvallis, OR 97331-5503. (email: ahuyer@oce.orst.edu; kosro@oce.orst.edu)

R. Lukas and P. Hacker, School of Ocean and Earth Science and Technology, University of Hawaii, Honolulu, HI 96822. (email: phacker@iniki.soest.hawaii.edu; rlukas@iniki.soest.hawaii.edu)

(Received June 28, 1996; revised November 21, 1996; accepted December 5, 1996.)